MOF-Derived Metal-Carbon Composite Materials as Bifunctional Catalyst for Zn-Air Battery

Artun Şanlı

Promotor:

Prof. Jan Fransaer

Assessor:

Priv. -Doz. Dipl.-Ing Dr. Stefan Steinlechner
Prof. Jef Vleugels

Daily supervisor:

Dr.Xuan Zhang

Foreword

This master thesis was carried out from September 2019 to January 2021 in the Department of Material Science of the Katholieke Universiteit Leuven, Belgium.

First and foremost, I would like to thank my promotor, Prof. Jan Fransaer for believing in me throughout my master thesis and providing me with the necessary information and feedback to complete this project. Moreover, I appreciate his patience and extreme understanding in the delay of this project while the whole globe is shocked with this unexpected and unprecedented pandemic.

Secondly, I am glad to have Dr. Xuan Zhang as my daily supervisor who has supported me with his unlimited knowledge during the whole process. His help and guidance were vital to me and without his support I would not be able to finish this work even in two years. I am also thankful to Wei Zhang and Wei Guo, as they have given their unconditional support in day-to-day activities and helped me out even after the midnight. I am really happy to work with them and learn from them. This was a great experience and I never regret a moment of this arduous but exciting journey.

Next, I am deeply grateful to all my professors and staff both in KU Leuven and MU Leoben. I am especially thankful for the support that I have received from Priv. -Doz. Dipl.-Ing Dr. Stefan Steinlechner, who has been supporting me throughout my whole study. It is worth mentioning here that the support I have received from EIT Academy is undeniable and I appreciate the generous moral and economical support that they have given me.

Lastly, I am really thankful to my family and all of the loved ones for believing in me and always supporting me. Their love and support made me brave enough to face all of the difficulties caused especially by being separated from them by thousands of kilometers.

Artun Şanlı

Contents

Abstract

Starting with the industrial revolution, global energy demand grew rapidly and fossil fuels began to be used to meet the energy demand. The consumption of fossil fuels increased rapidly with the improvement in technology and growth in population and thus became a treat to our environment. In order to replace fossil fuels with the green energy, alternative energy storage devices are necessary. Currently used Li-Ion batteries are far from satisfying the world's needs and metal-air batteries are promising candidates thanks to their high energy density (1084 Wh kg^{-1}) while utilizing one of the most abundant elements in the world, zinc. However, the necessary reactions for metal-air batteries--Oxygen Reducing Reaction (ORR) and Oxygen Evolution Reaction (OER)--are highly sluggish, and this delays the industrialization of metal-air batteries. Catalysts are strictly needed to guide these reactions and change their paths. Although some noble catalysts like, Pt for ORR and IrO_2 and RuO_2 for OER possess established efficiencies, these materials are rare and expensive, and thus are not optimal for industrialization but rather used for research purposes. Metal organic frameworks (MOFs) derived materials are alternative to noble catalysts, thanks to their high tunability, high surface area and hierarchical porous structure. MOF-derived materials often need high pyrolyzing temperatures for graphitization and also removal of metal centers. As an alternative Cd based MOF derived material is offered because of the low boiling temperature of Cd (767 ^{o}C). Cd MOF's were synthesized by various modulating ligand ratios and synthesis times which resulted in different morphologies and particle sizes. Zn-ZIF-8 with various modulating ligand ratios were also synthesized in order to obtain similar particle size for optimal comparison. Samples were pyrolyzed in different temperatures, temperatures that are higher and lower than Cd boiling temperature and characterized. ORR and OER measurements were executed to understand the catalytic performance of Cd and Zn samples. Pyrolyzed Cd samples have shown much smaller CV plot, which indicates lower double-layer capacitance thus much lower surface area. Despite having much lower surface areas, pyrolyzed Cd samples have shown better or similar catalytic performance in ORR and much smaller Tafel-slopes, which were on par with reference Pt/C catalyst. OER performances of the both samples were not good. The promising results gained from Cd catalysts have shown that more investigation is necessary to increase the surface area in order to be used in metal-air battery applications.

List of Figures

List of Tables

List of Abbreviations

2-mIm ---------- 2-methylimidazolate
CdIF-1 ---------- Cadmium 2-methlyimidazolate
CdIF-3 ---------- Cadmium 2-methlyimidazolate
CNM ---------- Carbon nano materials
CNT ---------- Carbon nano tubes
CV ---------- Cyclic voltammetry
EDS ---------- Energy dispersive spectrometer
EIS ---------- Electrochemical impedance spectroscopy
K-L ---------- Koutecky-Levich
LSV ---------- Linear sweep voltammetry
MOF ---------- Metal organic frameworks
OER ---------- Oxygen evolution reaction
ORR ---------- Oxygen reduction reaction
RDE ---------- Rotating disc electrode
RHE ---------- Reversible hydrogen electrode
SBU ---------- Secondary building unit
SEM ---------- Scanning electron microscopy
TEA ---------- Triethylamine
XRD ---------- X-ray diffraction
ZIF ---------- Zeolitic imidazolate frameworks
ZIF-8 ---------- Zinc-2-methylimidazole
ZIF-67 ---------- Cobalt-2-methlyimidazole

Chapter 1. Introduction

In the second half of the 18th century, the industrial revolution was started in the United Kingdom and the demand for energy increased rapidly. Since the beginning of this development and the increase in the world population, the energy need for devices was met mainly by fossil fuels. Fossil fuel burning is a major threat to the global environment by increasing the average global temperature and CO_2 concentration in the atmosphere [1] also threatening future generations [2] and the yield of major agricultural crops[3] etc. Because of these negative effects, environmental-friendly clean energy, so-called "green energy" is examined. Several kinds of renewable energy sources have recently begun to replace fossil fuels but the focus is given in to electrochemical energy storage devices, because of the newly emerging and expanding electrical vehicle market [4, 5] . Lithium-ion batteries are a great success after they entered the market in the late 90s. Continuous development is aimed to increase the energy and power density and it is believed that improvements in Li-ion technology can increase the energy density by 30% at most[6]. When limited expected improvement in Li-ion batteries added to the existing safety issues and problems regarding Li recycling, are created a new search for energy storage devices [7].

Metal-air batteries are the most promising candidates to replace older energy storage solutions because of their high theoretical densities, [8–11] low cost, compactness, light-weight and safety in handling [9, 12–14]. Metal-air batteries have taken the interest because of their higher theoretical density which is even a few times more than the best performing Li-ion batteries [15]. Metal-air batteries were researched much earlier than lithium-ion batteries and commercially entered the market in 1932. The abundant problems related to metal anodes, electrolytes and air electrodes however hampered their deployment [16]. Although Li-air batteries possess the highest theoretical energy density (5200 Wh kg^{-1})[17], Zn-air batteries are in the spotlight because of their cost, safety, abundance, and relatively high energy density (1084 Wh kg^{-1}), which is already four times higher than those of the best current Li-ion batteries [13, 18]. Air battery components are indicated earlier and the most complicated part is the air electrode which includes a gas diffusion layer and an oxygen electrocatalyst layer [19]. The ORR (Oxygen Reducing Reaction) taking place at the air electrode is performance-limiting in metal-air batteries because of the sluggish behavior of ORR [15]. In addition to that, the reverse reaction of ORR, OER (Oxygen Evolution Reaction), is a crucial reaction when the future of metal-air batteries is considered because it is the active reaction in the recharging process. Therefore, the creation of an air electrode that works as a catalyst in ORR and OER is a highly focused subject by the community. A lot of studies were conducted regards to ORR because it is happening in the discharge process but less attention was given to OER which occurs during the charging process.

Catalysts are strictly needed to achieve high reaction rates and they basically serve as a guide that can speed up and change the path of a chemical reaction. Several materials have an established efficiency, Pt for ORR and IrO_2 and RuO_2 for OER, which are quite rare in the earth's crust and fairly expensive. In addition to that, these two reactions have different characteristics and thus, materials that are currently used are not applicable for both reactions. Because of these reasons, a search for cheaper and better alternatives are active. Porous carbon catalysts are the most promising alternative because of their high chemical and mechanical stability, excellent tunability of pores and surface properties, good electrical conductivity and thermal stability, high surface area, and easy application on top of their low cost [20]. In general, most of the porous carbon materials can be produced with simple thermal decomposition and possess the properties mentioned above with a lack of irregularities in their pore sizes and connection, which severely prohibits their application. To prevent this, templates are introduced in the production process which can be separated as hard and soft templates. Hard templates are rigid and insoluble molds that already possess the desired pore structure. Although most of the porous carbons can be produced efficiently with this method, the technique is highly expensive and work-intensive which limits its used fields [20]. The soft-template method, on the other hand, can be applied to a limited number of samples because of the decomposition of organic matter in high temperatures which is needed for complete carbonization [20].

Recently, MOF (Metal-Organic Frameworks), constructed with metal ions and organic ligands, which can be seen in figure 1, are used as a sacrificial template in the creation of different carbon-based materials that include heteroatom-doped and metal oxide decorated porous carbons with the help of thermal decomposition under Ar and N_2 atmospheres to replace expensive catalysts. This production route enables scientists to obtain carbon-based materials with high surface areas and offers them extensive room to change the porosity and functionality of the material with other heteroatoms for each specific application. Thus, MOF-derived materials can be used in various fields such as energy, environment and medicine [20].

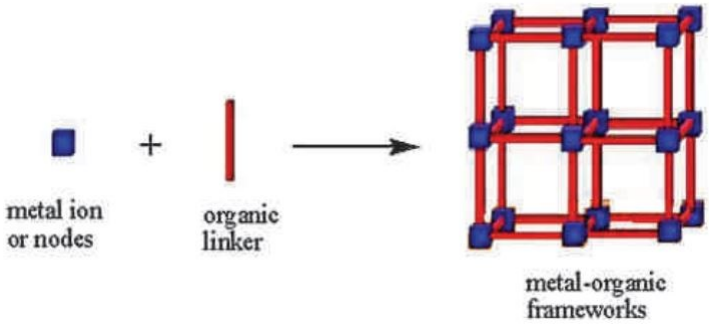

Figure 1: Components and structure of MOF's [21]

In most cases, a high surface area and hierarchical porous structure correlate with a good sacrificial MOF-derived material as an electrocatalyst. High-temperature thermal decomposition promotes a higher surface area with larger pores but also the destruction of ordered structures [20]. Because of this reason, a new type of sacrificial material that has a transition metal with a lower boiling temperature is investigated.

Chapter 2. Literature review

2.1. Metal-air batteries

2.1.1. Elements used in metal-air batteries

Metal-air batteries consist of five parts; a metal-based anode, an alkaline or salt-based electrolyte, a separator, an air cathode, and a gas diffusion layer which can be seen in figure 2. Oxygen is the active material in the positive electrode which is available in ambient air. The advantages of using oxygen as a cathode material comes from its highly oxidizing characteristics, light weight, and abundance. In addition to that, there is no need for cathode material and this leads to a fully packed battery with a metal-based anode. In order to use the full advantages of metal-air batteries, anode material needs to meet certain requirements [19]. Basically, it should have a strong reducing power to give high energy voltage, low molecular weight with high density and large valance change, and moreover, it should be abundant in nature and environment friendly.

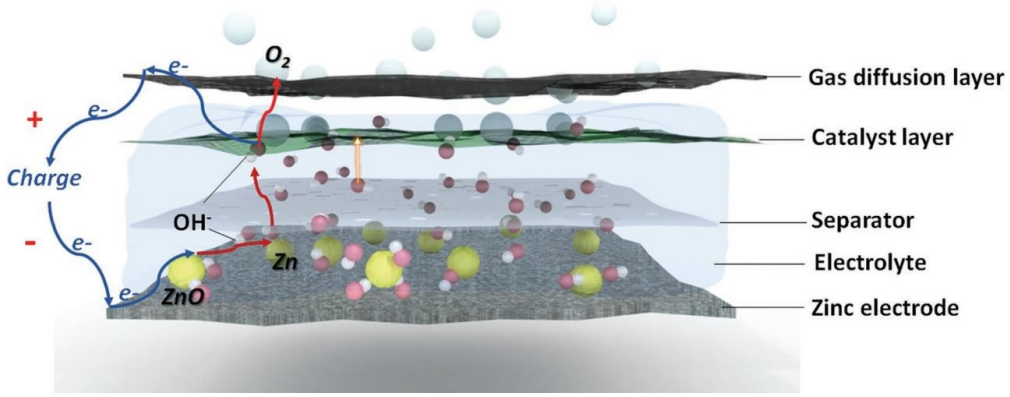

Figure 2: Schematic of an aqueous rechargeable zinc–air battery [7]

In recent years, lithium, aluminum, zinc, and iron-based metal-air battery have received much scientific attention. Theoretical energy densities of these materials are given in table 1 below. As the theoretical energy densities of Li and Al are much higher than that of Zn and Fe, these materials have attracted the attention of researchers and industries in the first place. Although Li-air batteries have the highest energy density, their high hazard potential in water containing environments and high cost due to limited lithium resources have critically impeded their commercialization [5, 22, 23].

Table 1: Theoretical energy densities for different types of metal-air batteries [7, 15]

Metal-air Batteries	Theoretical Energy Densities (Wh kg^{-1})	Volumetric Energy Densities (Wh L^{-1})
Lithium	11429	7989
Aluminum	8076	10347
Zinc	1353	6136
Iron	1229	3244

Aluminum is another option for metal-air batteries with high theoretical energy density and reducing power. In addition to its high energy density, it is the second most abundant element in the world after silicon and it is known for its non-toxicity and high recyclability [19]. Aluminum-air batteries have a short shelf life because of hydrogen evolution even under open-circuit conditions [24]. Electrolyte and negative electrode connections should only be established just prior to use because of the corrosive behavior of aluminum in alkaline aqueous solution as indicated in several papers. These drawbacks given for the Li and Al lead scientists to focus on other metals such as Zn.

Zinc is the only metal-air battery that is already commercialized. It is used in medical devices such as hearing aids and wireless messaging devices [25]. Zinc has less energy density when compared with Li and Al but overall more stable and because of that charging in aqueous electrolytes can be done more efficiently [7]. In addition to that, according to Cano et al., zinc metal has a relatively high volumetric energy density comparable to lithium-air which can be seen in table 1 with all the other elements. High volumetric density is crucial when new and compact technological devices are considered such as smartphones and electrical vehicles. Despite Li and Al, zinc can be used more safely especially in front of an automobile, which provides necessary oxygen supply to the air batteries while it is moving forward [7]. Zinc is also the fourth most abundant metal in the world, 300 times more than lithium (qtd. in Toussaint et al., 2010). According to the European Environment Agency's projection about electric vehicles in 2050, 80% of the vehicles will be electric and this will require much more material than demanded today [26]. For this purpose, more abundant, safer and higher capacity energy storage solutions are needed, and Zn-air batteries are the most promising alternative to focus on.

2.1.2. Charge and discharge mechanism of metal-air batteries

Metal-air batteries can be divided into two sub-categories depending on their charging mechanism, either mechanically or electronically. Mechanically charged metal-air batteries, also

called primary batteries, only discharge and after the full capacity of the battery is used, the zinc anode is replaced mechanically with a fresh one. On the other hand, in electronically charged metal-air batteries, also referred to as rechargeable/secondary batteries, both discharge and charge reactions happen and no intervention is needed during their lifetime. Mechanically charged metal-air batteries suffer from poor electrode reversibility and unstable bifunctional air electrodes, but it is costly to establish a network for zinc recharging and supplying [7]. Air electrodes suffer in the electrically recharging process because of the relatively high voltages [5, 7, 9].

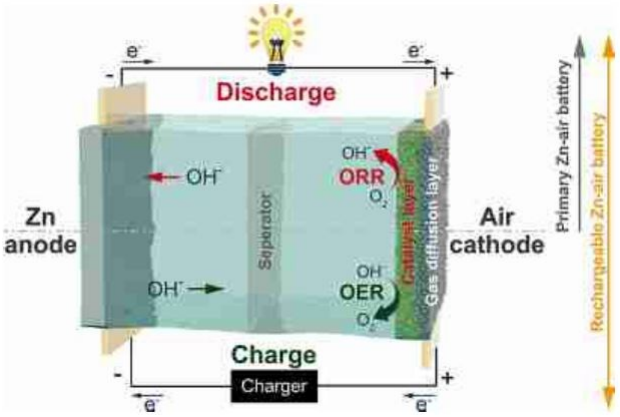

Figure 3: Charge and discharge mechanism of Zn-air battery [27]

As in the conventional batteries two separate reactions take place at different electrodes in the discharge process and it is performed only electronically. At the air electrode (cathode), oxygen from the atmosphere is dispersed into the electrode because of the oxygen pressure difference inside and outside [13]. This electrode is only permeable to oxygen, but to the electrolyte [28]. In ORR, oxygen tends to be in the gas phase because of its low solubility and diffusivity in alkaline electrolytes [5]. So a three-phase boundary is formed with, gas (air), liquid (electrolyte), and solid (catalyst), where ORR happens [5]. As the size of this boundary is increased, more oxygen is gained through the air. Representation of this zone is indicated in figure 4 with a red circle.

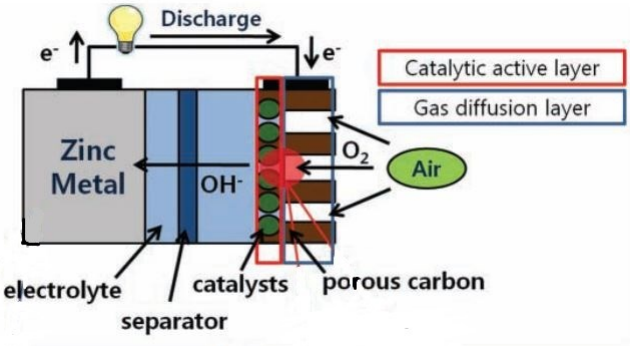

Figure 4: Three phase boundary in air cathode[13]

The hydroxide ions carried through the alkaline electrolyte oxidize the zinc metal on the anode side and the electrons generated are carried through an external connection to the positive electrode [13]. In the discharging step of Zn-air batteries, the reactions occurring in different electrodes can be listed as:

Anode:
$$Zn \leftrightharpoons Zn^{2+} + 2e^- \quad (1)$$
$$Zn^{2+} + 4OH^- \rightarrow Zn(OH)_4^{2-} \quad (2)$$
$$E° = -1.25\ V\ vs.SHE$$

Cathode:
$$O_2 + 2H_2O + 4e^- \rightarrow 4OH^- \quad (3)$$
$$E° = 0.4\ V\ vs.NHE$$

Overall Reaction:
$$2Zn + O_2 \rightarrow 2ZnO \qquad E° = 1.65\ V\ vs.SHE \quad (4)$$

Practical working voltages of zinc-air batteries are lower than 1.65 V as a result of the internal energy loss [13]. Because of that, the obtained energy density is in the range of 350 – 500 Wh/kg [15]. This value is limited because of the inefficiency of the air cathode and it is therefore not applicable for commercial use. They are commercially available in only low power requiring applications such as hearing aids.

The difference between these two configurations of batteries is already mentioned in anode stand point and a representation can be seen in figure 5. Other than that, they also differ in air electrode. In rechargeable metal-air batteries, the OER and ORR take place in the cathode whereas in primary batteries only the ORR reaction occurs in the cathode, which will be discussed in detail in the following section.

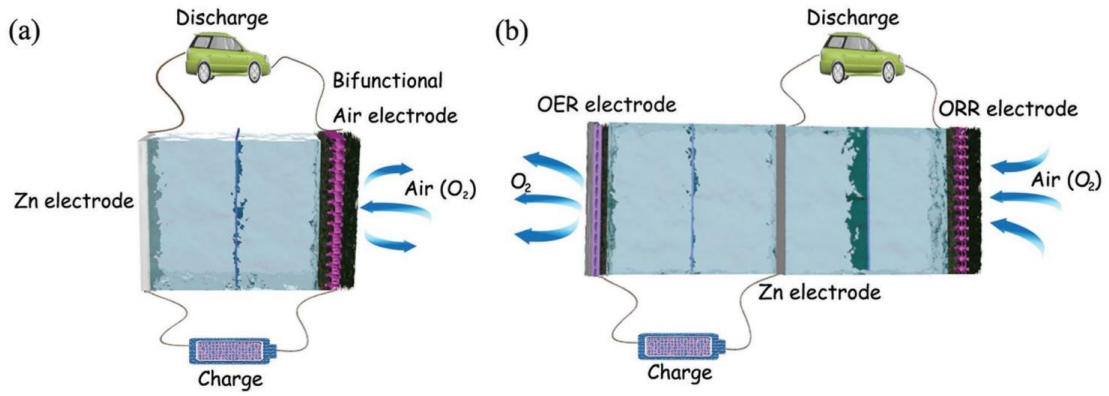

Figure 5: Two zinc-air battery configuration [5]

2.2. Oxygen Reducing Reaction

ORR is heavily investigated because of the importance of converting energy especially in metal-air batteries and fuel cells [29]. The performance of rechargeable zinc air battery is heavily affected by both the ORR and OER as it is seen from figure 6, which represents the polarization curves of zinc-air batteries. Anode overpotentials are significantly smaller than cathode overpotentials. The green arrow shows the overpotential of ORR and because of that, practical voltages are much smaller than the theoretical voltage (1.65 V). In order to produce an effective catalyst for ORR and OER, firstly the reaction kinetics, electron pathways, and the overpotential behavior need to be identified.

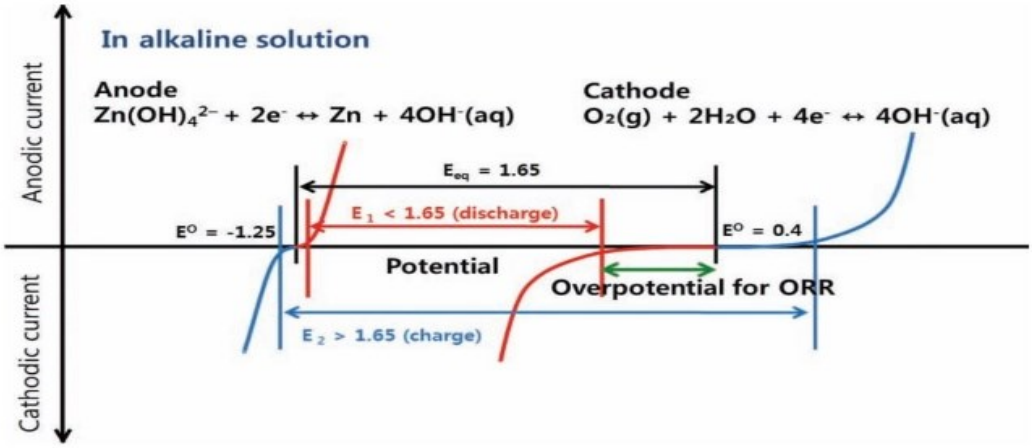

Figure 6: Schematic polarization curves of zinc-air cell. Black line represents the equilibrium potential (1.65 V), red and blue lines are discharge (>1.65 V) and discharge (<1.65 V) respectively [13]

2.2.1. Kinetics

Oxygen reducing reaction is largely investigated because of the energy convergence capacities and use of it in sustainable energy storage devices. The reduction mechanism has two possible pathways which are either 4 electron route from O_2 to H_2O or 2 electron route from O_2 to H_2O_2. This mechanism was firstly introduced by Damjanovic et al. and modified by Wroblowa et al., to simplify complex reaction pathways that are mentioned [29]. Reaction components and the end products depend on the pH of the environment. In both media, 4 electron pathway is preferred. Schematic pathways for ORR on N-doped carbon materials are given in figure 7 below.

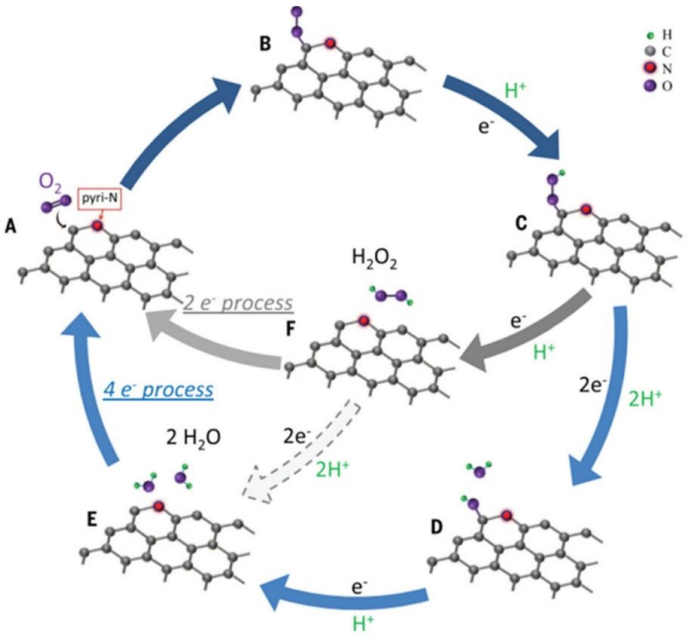

Figure 7: Schematic pathway of ORR on N-dope carbon materials [30]

In ORR, 4 electron pathway is preferred because of the efficiency gain in two-fold mechanism when it is compared with partial two-electron mechanism in 2 electron pathway [31]. The reactions for both routes in acidic and basic media can be given as follows:

In alkaline media:

4 electron pathway:

$$O_2 + 2H_2O + 4e^- \rightarrow 4OH^- \; E^o = 0.401\,V\; vs.SHE \quad (5)$$

Peroxide pathway:

$$O_2 + H_2O + 2e^- \rightarrow HO_2^- + OH^- \; E^o = -0.065\,V\; vs.SHE \quad (6)$$

$$HO_2^- + H_2O + 2e^- \rightarrow 3OH^- \; E^o = 0.867\,V\; vs.SHE \quad (7)$$

In acidic media:

4 electron pathway:

$$O_2 + 4H^+ + 4e^- \rightarrow 2H_2O \; E^o = 1.229\,V\; vs.SHE \quad (8)$$

Peroxide pathway:

$$O_2 + 2H^+ + 2e^- \rightarrow H_2O_2 \; E^o = 0.67\,V\; vs.SHE \quad (9)$$

$$H_2O_2 + 2H^+ + 2e^- \rightarrow 2H_2O \; E^o = 1.77\,V\; vs.SHE \quad (10)$$

Thermodynamic potentials of the reactions are given above are theoretical limits for these specific reactions. Recharging efficiency is highly dependent on the difference between the actual and theoretical potentials and the aim is to minimize it. In order to achieve that, kinetics of ORR

reaction must be fast [29]. As described earlier, the kinetics of metal-air cathodes is slow and it shows overpotential, which is expressed with η.

$$\eta = E - E_{eq} \quad (11)$$

Where E is actual potential and E_{eq} is equilibrium potential. Overpotential also consists of few parts and they are represented in equation 12.

$$\eta = \eta_{act} + \eta_{conc} + iR \quad (12)$$

η_{act} is activation overpotential, and it describes charge transfer kinetics of the reaction [29]. It is available in every reaction and dominant at low polarization currents.

η_{conc} is concentration overpotential and it is related to the limitations in mass transport and dominant for high polarization currents [29].

iR is ohmic drop and it is electronical resistivity when corrosion happens in the reacting anode and cathode product [29].

Equation that is related with overpotential is expressed in equation 13 and it is called Butler-Volmer equation [29]. The right side of the equation represents the cathodic branch since cathodic currents are negative.

$$I_c = i^o_{O_2} \left(e^{\frac{n_{aO} a_O F \eta_c}{RT}} - e^{\frac{n_{aO}(1-a_O) F \eta_c}{RT}}\right) \quad (13)$$

Where I_c is the oxygen reduction reaction current density, $i^o_{O^2}$ is the exchange current density, n_{aO} is the number of electrons transferred in the rate determining step, a_O is the transfer coefficient, η_c is the overpotential of ORR, F is the Faraday constant, R is the gas constant and T is the temperature in Kelvin. In order to obtain high currents at low overpotential either $i^o_{O^2}$ value should be large or $\frac{RT}{n_{aO} a_O F}$ should be small [32].

At large overpotentials, the right side of the equation, reverse reaction, can be neglected and the simplified version can be written as:

$$I_c = i^o_{O^2}\, e^{\frac{n_{aO} a_O F \eta_c}{RT}} \quad (14)$$

When this equation is written in logarithmic form, it gives a linear plot which has the slope of -$\frac{2.303RT}{n_{aO}\, a_O F}$, and called Tafel slope. When it is simplified like this, only variables are the transfer coefficient and the number of transferred electrons. In the case of ORR, two Tafel slopes are plotted using 60 mV/dec and 120 mV/dec, which depend on the used electrode materials [32]. High

Tafel slope means that over potential increases faster with the current density, and to obtain high current densities with low overpotential, a_0 and n_{a0} values should be high. Electron transfer coefficient is an important parameter in Tafel slope and it increases linearly with the temperature. In addition to that, this also explains why 4 electron pathway is preferred since it will decrease the Tafel slope by half when it is compared with the 2 electron pathway.

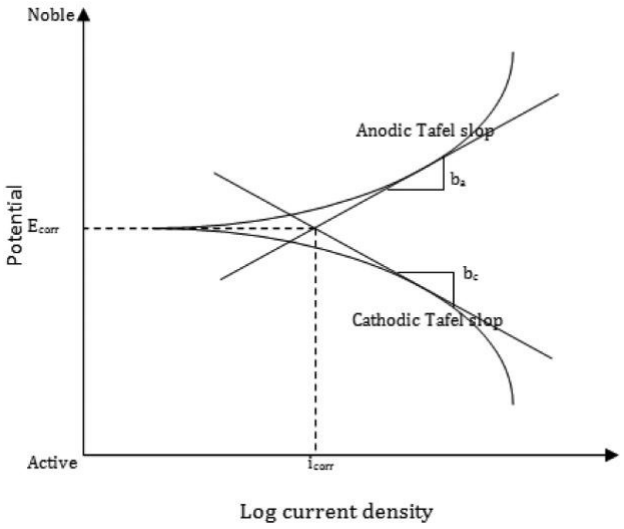

Figure 8: Hypothetical Tafel Plot [33]

Electron exchange current density is crucial when electrochemical reaction rate is considered. It is called exchange because reaction can happen in both directions. The magnitude of this reaction represents how quickly the reaction will occur.
The exchange electron current density depends on the reaction surface and the reaction itself. The materials that are used in ORR reaction also have a major effect. Traditionally, noble metals such as Pt or Au are used for such an application because the O_2 reduction reaction presents higher exchange current density.

The true electrode area and concentration of the reactant are other important factors that need to be taken into account [32]. Especially MOF-derived materials create a huge difference in electrode area when they are compared with the regular noble metals that are used as electrocatalyst and will be mentioned in more detail in further sections.

2.2.2. Electrocatalyst for ORR

The kinetics that are mentioned above for the ORR at the cathode are important because it effects the performance of metal-air batteries and fuel cells. There are several issues regarding that topic and they are well researched in the literature. Slow reaction kinetics and fuel crossover are two

of the important ones. An electrocatalyst which favors the four-electron reduction pathway from O_2 to water is needed. Pt is used as an ORR catalyst because of its activity and stability throughout cycles, however, the commercial applications are limited due to low cycling ability when it is compared with Li-ion and also the high cost. Although Pt is the best element for ORR, it still presents overpotentials more than 400 mV from equilibrium reversible potentials, which ends with oxide species formation on the Pt surface and hindering the performance [34]. Some of the electrocatalysts were heavily investigated and Pt group elements such as Pd, Ru and Ir are upfront. Other than these, some metal oxides with perovskite or pyrochlore structure, Pt doped CNT and transition element clusters with organic ligands, like MOF's are investigated to be used as an electrocatalyst in ORR applications [35].

2.2.3. Techniques to Investigate ORR and OER

Techniques that are often used in ORR studies are cyclic voltammetry, steady-state polarization and rotating disc electrode (RDE)

Cyclic Voltammetry (CV)

It is one of the easiest and most comprehensive techniques that are used in electrochemistry. This technique records the current that is developed in a cell where a potential is applied to a working electrode at a constant scanning rate in forward and reverse directions as a cycle.

A voltammogram typically shows a "duck" like shape because of the Nernst equation, which describes the equilibrium. Nernst equation relates electrochemical cell potential to standard potential of species and their individual activities [36]. Eqn.15 shows the Nernst equation:

$$E = E^0 + \frac{RT}{nF} \ln \frac{(Ox)}{(Red)} \quad (15)$$

Elgrishi et al. claimed that "The Nernst equation provides a powerful way to predict how a system will respond to a change of concentration of species in solution or a change in the electrode potential." Equation states when the E^0 is applied to a Me^+ solution, the Me^+ is reduced until concentration equilibrium is reached as Me = Me^+. When negative potential is applied to the solution, Me^+ is reduced to Me and as a result of that, Me^+ is depleted to the surface of the electrode. This process continues until the cathodic current peak is reached. After that, diffusion of Me^+ is achieved by bulk solution in where mass transport slowed down because of the diffusion layer created by Me. As diffusion gets slower, the current shows a decrease until the switching point. When the scan reaches the switching point, it is reversed in anodic direction and this time Me is depleted to the surface of the electrode. Peak currents act differently when voltages are applied

and the voltammogram shows a duck-like shape because of the separation of peaks. Peak difference is 59 mV when the electron transfer barrier is low which indicates that reaction is reversible. High electron transfer barrier indicates irreversibility which requires more negative potentials and thus the difference in peaks is more than 59 mV. Other than peak difference, scan rate is another parameter in the cyclovoltammetry applications which represents how fast the applied potentials change in a controlled environment. The higher the scan rate is, the smaller diffusion layer is created and thus higher currents are observed [37].

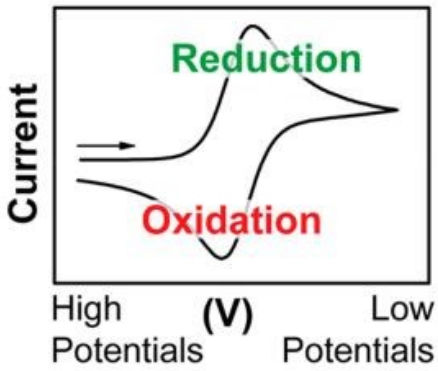

Figure 9: Cyclic Voltammetry Profile [36]

The cyclic voltammetry gives valuable and fast information about the reactions and catalysis. In specific, electrochemical properties of an analyte solution and some catalyst material properties such as surface area can be obtained by using CV measurements.

Steady-State Polarization

Polarization indicates that the equilibrium is shifted away because of a change in the potential of the electrode, which leads to an electrochemical reaction. Polarization is followed by the Butler-Volmer equation, which is given as Eq. 13. Especially in multi electron transfer reactions, overall reaction possesses multiple steps in which they have different Butler-Volmer equations. The whole reaction rate is determined by the slowest step and called "pseudo-elementary step with an electron transfer number *n* [32].

According to Song et al., "A steady-state polarization curve describes the relationship between the electrode potential and the current density, which is recorded by either holding the electrode potential and recording the stable current response, or holding the current density and recording the stable potential response" [32]. In ORR application, as it is discussed earlier, high current densities are expected at lower overpotentials. A typical polarization curve and appropriate zones are shown in Fig. 10.

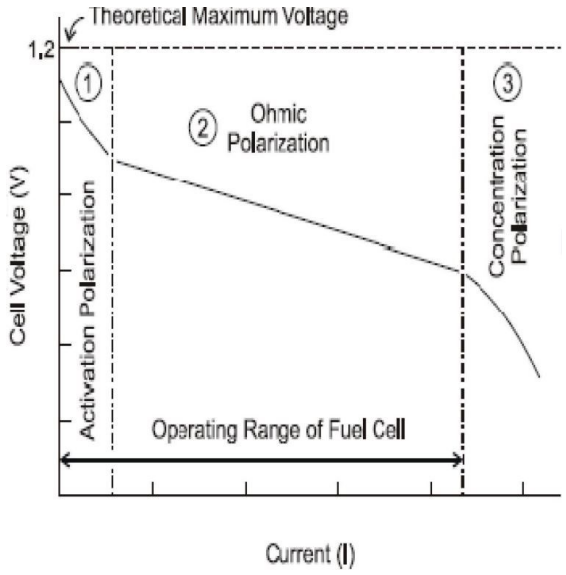

Figure 10: Polarization curve and appropriate zones [29]

The curve is recorded using potentiostat/galvanostat which measures the current when the desired voltage is applied. At lower currents, the potential is dropped because of activation polarization and at medium current levels potential is dropped because of the ohmic losses. At higher currents, the curve loses its linear behavior and starts to drop more rapidly because of concentration polarization.

The bottleneck of this discharge process is considered as ORR because of the different possible paths of the reaction.

Rotating Disc Electrode (RDE)

In ORR, it is highly important to design a setup to measure the reactant transportation to the electrode and understand its effects on electron-transfer kinetics [38]. The rotating disc electrode method is a widely used technique that consists of a circular conductive electrode material placed inside of an insulator. As the name implies, the rotating disc electrode can rotate at various speeds, which is described as ω. The rotation action is highly important to control the diffusion layer, which becomes thicker on top of the electrode when the rotation is absent, leading to an increased reaction time [38]. As a result, the obtained current density will be non-steady. High ω creates a thinner diffusion layer and thus higher currents can be measured. A representation of the RDE is given in the figure below.

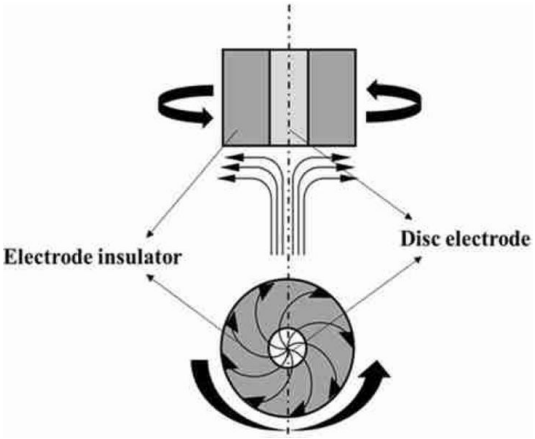

Figure 11: Rotating Disc Electrode [39]

The rotating disc enables to measure the diffusion coefficient and transfer kinetics of oxidant reduction, and when the kinetics of reduction reaches a rapid state, diffusion process is unable to keep up with electron transfer and leads to a straight line Levich plot when different rotation speeds are used [38]. The slope of the obtained straight line is given in the Koutecky-Levich equation as follows:

$$B = 0.62nFD^{\frac{2}{3}}v^{-\frac{1}{6}}c_0 \quad (16)$$

Where F is Faraday constant (96,485 C mol^{-1}), D is the diffusion coefficient of O_2 in the chosen electrolyte and v is the kinematic viscosity of the electrolyte. All values beside n, which is electron transfer number, are known and thus electron transfer number can be calculated with the given formula which helps to understand the ORR paths to determine the efficiency of the catalyst used.

2.3. Oxygen Evolution Reaction

2.3.1. Kinetics

Oxygen evolution reaction is the reverse reaction of ORR in which, O_2, H^+ and H_2O are produced depending on the pH of the media. Half equations corresponding to the media are given below:

$$4OH^- \rightarrow 2H_2O + O_2 + 4e^- \; E^o = 0.404V \quad (17)$$

$$2H_2O \rightarrow 4H^+ + O_2 + 4e^- \; E^o = 1.23V \quad (18)$$

In OER, 4 electrons are transferred by multi-step reaction just like for ORR but it only happens by a single electron transfer which makes OER more sluggish and results in higher over potentials

[40]. Equations given for ORR can also be applied to OER because basically they are opposite reactions. Moreover, the techniques that are detailed for ORR are also used for OER. Although they have many similarities, the used catalysts need to have different properties. A more robust structure is needed for OER because of the higher voltages applied during the charging process [5].

2.3.2. Electrocatalyst for OER

As it was the case in ORR, noble metals are primarily used in OER, Ir and Ru shows better performances in OER, rather than Pt and Pd [5, 40]. Their oxides show low overpotentials and excellent stability in the charging process, which makes these metals harder to replace, although they are rarer and more expensive than the other options.

The research is focusing on replacing these expensive noble metals with more abundant metals or carbon-based materials in order to make them viable for industrial applications. Mainly oxides, perovskite structures, nitrogen-doped structures are investigated.

2.4. Metal Organic Frameworks

2.4.1. Introduction

The Metal-organic framework concept was firstly introduced by Tomic in 1965 and attracted many researchers and scientists as a porous material and the term was first used by Yaghi in 1995 [41]. MOF is constructed with oxo metal clusters, which contain a central metal atom and oxygen ligands such as O_2, and OH, linked by organic ligands and classified as porous organic-inorganic hybrid materials. As mentioned, the structure is formed by organic linkers and metal clusters and it can be seen in figure 1. Organic linkers are referred to as SBU (secondary building units), which act as a “strut” but metal clusters are referred as inorganic SBU and act like a “joint”. This type of structure offers high porosity and very large surface areas that make them suitable for energy conversion and storage, heterogeneous catalysis and gas separation applications. Possible applications can be seen in figure 12.

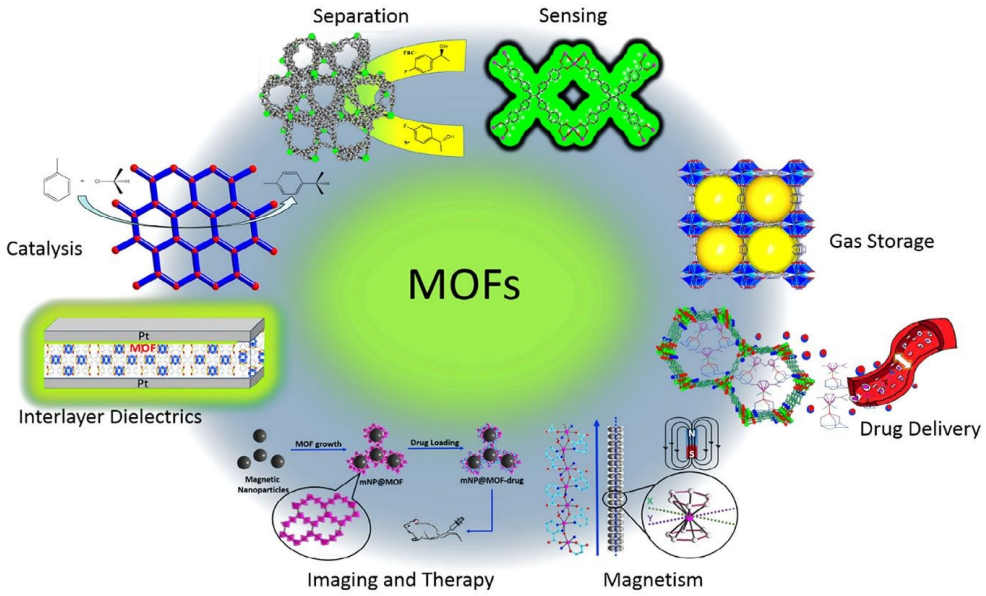

Figure 12: Myriad applications of metal–organic frameworks make them promising future materials [42]

Although the porous MOF concept was introduced in 1965, development and synthesis of MOF's are delayed because of lack of information about the synthesis which limited the variety of structures [43]. The currently discussed methods of using MOF's were developed by O.M. Yaghi 25 years ago, which is used for selective binding and removal of specific molecules by MOF's [44]. Now, more than 20,000 MOF's are reported with combinations of metal clusters, ligands and in various 0D, 1D, 2D, 3D morphologies [45].

2.4.2. MOF derived materials

The distinct morphology and modification of compositions enables MOFs to functiom as a perfect template for nanostructures creation by using high-temperature pyrolysis[46]. Earlier investigation revealed that MOFs are very likely to collapse and thus to suffer damage to their morphologies that makes them featureless in under harsh and high temperature environment [47]. Since MOFs are heavily investigated, more appropriate precursor materials and controlling mechanisms for pyrolysis are selected to prevent the morphological damages and also to obtain a wide range of morphologies. Pyrolysis of MOFs also stands out with the other synthetic nanostructure production approaches because it allows controlling several parameters (size, shape, composition and structure) with variable temperatures and pyrolysis atmosphere while enabling a variety of functions to be added in a single step [20, 46].

Production of MOF-derived materials can be separated into two different methods which are self-templating and external-templating methods. As the name implies, self-templating method consists of only MOF products and the external-templating method utilizes soft and hard external

templates such as graphene and carbon [46, 48]. The method to choose depends on the provided features as well as the advantages and the disadvantages that they bring. According to Lah et al., self-templating and external-templating methods provide spherical and single-crystalline structures for hollow MOF's but these methods have different advantages and disadvantages [48]. The advantages of self-templating methods are no requirement for an external template and etching process while external templating methods provides facile synthesis and diverse template surface modifications [48]. On the contrary, self-templating method may have some difficulties in finding proper conditions and external templating methods often have no morphology control [48]. As mentioned in the previous section, MOF's have various morphologies in 0D, 1D, 2D, 3D. The classification of materials as regards to their dimension is derived from their number of dimensions that they have larger than 100 nm. So, within that definition, 0D materials have all dimensions smaller than 100 nm and 3D materials have all dimensions bigger than 100 nm. 0D materials have polyhedral, hollow and core-shell nanostructure which needs to be preserved in thermal transformation and thus requires high thermal stabilities [46]. As an example, ZIF's have high thermal stabilities up to 550° C in N_2 atmosphere which enables them to be converted without any change in their morphology [46]. The thermal treatment of ZIF precursors, which are polyhedral, creates structures with countless active sites and thus can be used in electrocatalytic applications. Despite the fact that 0D structures have large surface areas, full control in porosity is still not achieved because of their small size. 1D structures are typically nanorods and nanotubes and they have similar features with 0D and 2D nanosheets, which can be produced with both self-templating and external-templating methods. Like the 0D structure, only few MOF precursors are appropriate for self-templating methods and often include Fe-, Co- or Ni- in order to be assisted by their catalytic properties [46]. 1D structures tend to be used in sensing applications because of their uniformity of high active species which expedites the mass production. 2D structures are layer-like structures which include nanosheets and nanoflakes. These structures can be obtained basically by exfoliation of 1D structure into a layer. 3D structures are offering much more surface areas when they are compared with the lower dimensioned structures [46]. A large variety of structures are available within this group and they are arrays, flowers, honeycombs and sponges [46]. 3D structures can also be knitted with 1D nanotubes into desired shapes [46].

2.4.3. Zeolite Imidazolate Framework

MOF's show similarities with another class of porous materials known as zeolites [43]. Zeolites are one of the most important synthetic products for humanity and the main application areas include catalyst in petroleum refining and water softeners in detergents which had an approximate value

of 350 billion dollars in 2009 and it is increasing every year [49]. Zeolites are the most favored electrocatalyst in commercial applications because of their pure inorganic structure, which provides the necessary robustness that is needed under extreme conditions. A drawback of zeolites is that they prohibit close control in size, shape and functionality, which is in stark contrast to MOF [50]. The main advantage of MOF's over zeolites is their wider chemical variety due to the organic component. Although great variation of MOFs with good thermal stability are possible, they are far behind zeolites in that matter which makes them suitable for milder environments. Apart from zeolites, which possess high surface area, MOF's have the flexibility of pore design with controlled structure and functionality of the pores [51].

It is discovered that, the preferred angle (145°) of Si-O-Si in zeolites is the same as the bridging angle of M-Im-M which enables to synthesize zeolite imidazolate frameworks (ZIF) [49]. In recent years, thousands of MOF were synthesized and ZIF are one of the MOF classes. ZIF can be obtained from tetrahedral Zn and Co metal clusters (MN_4), M as Zn and Co, with a simple imidazolate linker [52, 53]. Banerjee et al. stated that there were 25 different ZIF's with different imidazolate linkers and Zn, Co nitrates in 2008 and it is known that there are at least 100 different ZIF structures are present [49, 54]. Topologically, ZIF's are isomorphous to zeolites but more importantly, possess other advantages such as high porosity (1821 m^2/g^{-1}), high thermal resistivity (up to 550° C) and relatively good chemical stability, which make them suitable for gas separation and catalysis applications [55]. ZIF's are therefore considered a promising replacement for zeolitic catalyst and a template with high surface area.

One of the most common ZIF structures called ZIF-8 is chemically represented as $Zn(mIM)_2$, where m is Zn and IM is imidazolate linker, has a rhombic dodecahedron morphology. Zinc MOF's are receiving attention as a sacrificial material to secure a high porous carbon-based matrix because of its relatively low boiling temperature (908° C). In addition, it shows high thermal stability with good electrical conductivity, which is useful in energy storage applications.

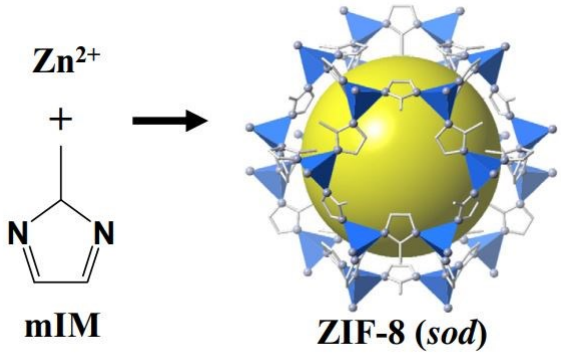

Figure 13:Crystal structure of ZIF-8: Zn (polyhedral), N (sphere), and C (line) [54, 56]

The interesting thing about this structure is that Zn atoms can be replaced with other metals. Co was done firstly and referred to as ZIF-67 [53, 57]. Substitution of zinc nodes with other metals while maintaining the sodalite structure is important not just from a scientific standpoint but also for engineering applications [58]. Partial substitutions of zinc nodes with catalytically active metals convert inactive ZIF to an active one [59, 60]. Another benefit is obtained when the substitution amount is accurately controlled, which enables fine tuning of the effective aperture size [61]. ZIF-8 with Cu^{2+} substitute presents superb catalytic activity and chemical stability while it requires excessive amounts to be substituted [59, 62]. Moreover, further doping of Cu^{2+} resulted as a complete collapse of ZIF structure [59]. It is stated that Co/Zn bimetallic ZIF exhibits much better stability when it is compared with the single metal ZIF [63]. Besides cobalt and copper, nickel, magnesium and manganese can also be doped to a ZIF-8 structure [61, 64]. However, Mg and Mn doping requires inert gas (Argon) conditions because of their unstable nature in ambient conditions and expensive reactants. The real challenge for substitution is that the ZIF-8 structure requires a non-distorted tetrahedral M-N_4 coordination [64].

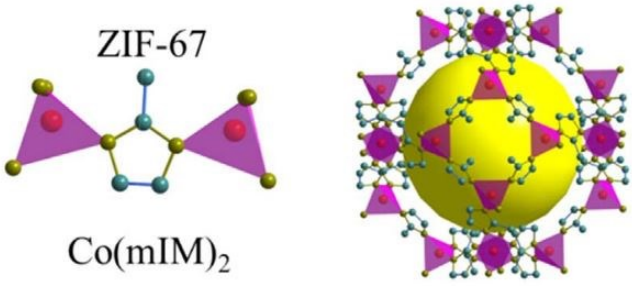

Figure 14: Crystal Structure of Zif-67 [65]

Cadmium is another metal that can be used in substitution of Zn in a ZIF structure, which has a few synthesizing protocols in the literature. Cd is in the same elemental group so possesses similar properties to Zn. Cd-ZIF-8 is called CdIF-1 in the literature and shows more stability than others

listed above and it has gained greater popularity in engineering applications but synthesizing requires a much narrower window which can bear phase transformations more easily [58]. In addition to that, synthesizing pure CdIF-1 requires an organic deprotonator like TEA (triethylamine) rather than inorganic deprotonator sodium formate which is typically used in Zn-Co-ZIF's, in order to form ZIF powders [58]. Deprotonation of ligands in CdIF-1 synthesis is more critical in creating stronger energy barrier because Cd^{2+} ions can be found in octahedral coordination but as mentioned earlier, tetrahedral coordination is required to have ZIF-8 structure [58, 66]. Sun et al. developed a protocol to synthesize pure Cd-ZIF-8 solvothermally with various TEA amounts and found out that TEA is not just critical for CdIF-1 synthesis but also provides some resistance in phase transformation. Without sufficient amounts, phase transformation to CdIF-3 or other unknown phases can be experienced [58].

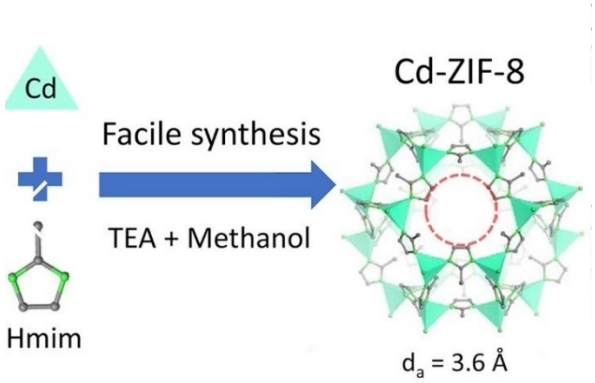

Figure 15: Crystal Structure of CdIF-1 (Cd-Zif-8) [58]

2.5. ZIF as a Sacrificial Material for Electrocatalysts

As mentioned in the previous chapters, platinum group elements are used mainly as a catalyst in ORR and OER, which makes the Zn-air batteries harder to implement in industrial applications and replace the currently used Li-ion batteries. As a hybrid material, ZIF's possess excellent tuning properties, high surface area, good chemical and thermal stability but lack electrical conductivity and thus, it is unsuitable to be applied directly to an air battery system but it would be a great candidate as a precursor for electrocatalyst with the desired unique properties [67]. The major advantages to using ZIF as a sacrificial material for electrochemical applications are given by Liu et al. and these are; high electrically conductive carbon matrix created from organic framework, heteroatom doping that is available in the organic ligand to create more active sites, in situ synthesis of carbon matrix with transition metals homogenously distributed in the framework,

well defined and adjusted parameters such as morphology and particle size and lastly preserved features inherited from precursor materials [68].

To increase the conductivity, CNM (carbon nano materials) are required. Graphene sheets is an excellent support material for catalyst with a large surface area, high conductivity and good thermal and chemical stability [18]. One study shows that graphene sheets supported Pt catalyst was superior in catalytic activity and stability when it was compared with the unsupported Pt catalyst, which emphasized the effect of carbon materials [69]. Another example of using graphene as a support material is incorporation with spinel electrocatalyst such as Co_3O_4 and $NiCo_2O_4$ which has shown comparable ORR performances with Pt/C catalyst and much better OER performance [18, 70].

In the case of MOF's and ZIF's, carbon structures are created with pyrolyzing in medium (700 ° C-1000° C) to high (1200° C-2000° C) temperatures [71–75]. ZIF's are excellent pristine material to start because of high C and N content; C facilitates conductivity and MN_4 molecules are known to be an active site for ORR [10, 72, 73] . Required conductivity is achieved by the conversion of stable domains, such as benzene rings, into carbonaceous structures starting from 500° C graphitic carbon around 800-900° C, which creates CNT (Carbon Nano Tubes) [10, 76]. Direct pyrolysis of ZIF's decomposes structure thermally and distributes metal-nitrogen active sites uniformly to porous structure [73, 76].

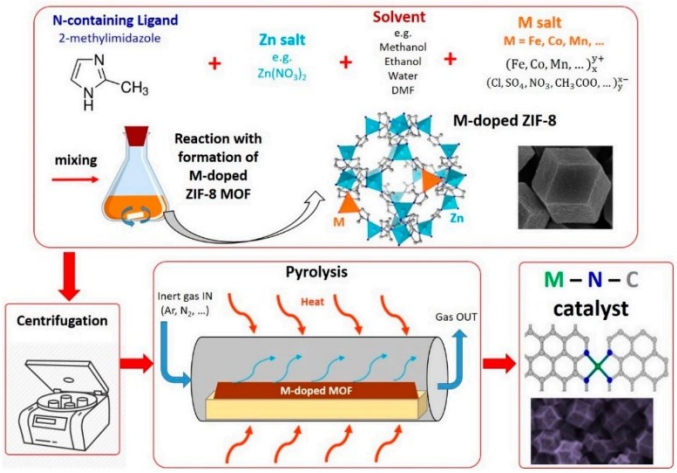

Figure 16: Schematic representation of M-N-C bi-catalyst using a pyrolyzed ZIF [77]

Figure 16 shows an overall bi-catalyst production route from pyrolyzed ZIF. The process starts with solvothermal synthesis of ZIF with metal salts and organic ligands are followed by pyrolysis under an inert gas such as (Ar, N_2, H_2) [71–73].

Prior to pyrolysis, ZIF has a high surface area, due to being microporous and often facilitates aggregation that reduces the active sites and blocks the mass transfer [71]. Pyrolysis facilitates the

decomposition of the carbon structures and also vacates the metals, and thus increases the pore size and decreases the surface area (1616 m^2/g vs 513 m^2/g) [72]. Moreover, N_2 absorption test applied has shown some hysteresis after pyrolysis which indicates hierarchically porous structure [67, 71]. Hierarchical morphology creates strategical channels and pore sizes as well as catalytic active sites that are beneficial for processes like ORR [67, 71].

In low pyrolysis temperatures (600° C), specific area, metal and nitrogen content are much higher when compared with the higher temperatures which are all beneficial for catalytic activity but lack of graphitization at low temperatures hinders positive attributes. Increasing pyrolysis temperature increases graphitization but lowers the specific area, metal and nitrogen content. In the case of ZIF-67, pyrolysis is executed in various temperatures (600° C-2000° C) and the sample which is pyrolyzed at 800° C outperforms the others [73]. The reason behind these results stem from the graphitization degree, nitrogen and metal content, surface area and also structural integrity. 800° C sample shows a reasonable graphitization and also a larger nitrogen and metal content with a larger surface area [72, 73]. Various authors indicate that overheating (around 1000° C-1100° C) the ZIF will result in the decomposition of the dopants and destroy the structure [10, 73].

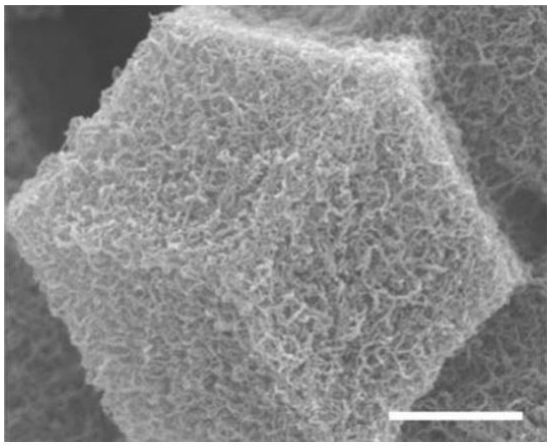

Figure 17: FESEM image of ZIF-67 pyrolyzed at 900 °C, the scale bar is 500 nm [72]

Inert gas is also an important factor in the determination of the end product. Xia et al. pyrolyzed the ZIF-67 particles in an Ar/H_2 atmosphere and maintained the cubic morphology while creating carbon nano tube frameworks [72, 76]. The presence of H_2 leads to open voids, which is an indication of hollow structure and this structure cannot be observed when just Ar is used as an inert gas [72]. The formation of CNT are also not parallel in one direction thus, abundant edges are formed, which increases the catalytically active surfaces [72].

2.6 Challenges

In the past 20 years, MOF-derived electrocatalysts have shown great improvement. They perform much better than the industrial standards which are Pt for ORR and IrO_2 for OER while preserving their bi-catalyst characteristics. Moreover, the electron pathway for these reactions is close to 4 electrons, which is preferred. On the other hand, there are several areas which require improvement and thus can be considered as challenges. First of all, the ORR and OER experiment conditions are optimized to give better results. For example, KOH concentrations are set to be 0.1-1 M, although it is widely used as 6 M KOH [9, 70, 78]. A lower concentration leads to a higher oxygen solubility which is in favor of battery performance [27]. Thus, oxygen diffusion should be improved in order to give closer results with the real-world applications. This might be achieved via surface engineering by optimizing surface wetting characteristics [27]. The other optimized experiment condition is the applied low current densities which are in the range of 10 mA cm^{-2} – 25 mA cm^{-2} [70, 78]. High current densities are required to power energy demanding devices in real life and this makes it essential to test batteries before fabrication. As a result, high current densities can result in the degradation of catalysts and dendrite formation in Zn anode. More stable bi-catalysts will endure in higher current densities and make it more applicable. The final challenge is the overpotential in the charging state. Higher overpotential is detrimental to the lifetime of the Zn-air batteries which are far behind the Li-Ion. Advance designs with increased oxygen reactivities and lower interfacial resistances are necessary to obtain better results [27].

2.7 Conclusion

Based on the information given above, this thesis attempts to explore the ORR and OER behavior of Cd-ZIF MOF derived catalyst, for which no example was found in the literature. Since the boiling temperature of Cd (767° C) is lower than Zn (907° C), the effect of lower pyrolyzing temperatures on the catalyst will be observed and compared with the ones which use ZIF-8 and ZIF-67 based catalysts. A larger surface area of Cd-ZIF is expected because of the larger surface area of pristine Cd-ZIF and also lower pyrolyzing temperature. In following works, particle size and morphology of ZIF's will be explored. The microstructure and chemical composition samples will be examined by the scanning electron microscope (SEM) and energy-dispersive X-ray spectroscopy (EDS). The crystalline structure will be examined by X-ray diffraction (XRD). The electrochemical performance of the end product will be tested by the CV and LSV methods and compared with the reference catalyst, which is Pt/C.

Chapter 3. Synthesis of Zn-ZIF-8 and CdIF-1 particles

3.1 Zn-ZIF-8 synthesis with room-temperature method

ZIF-8 particles can be produced with different techniques in which some of them are efficient and easy to control. The room-temperature synthesis method is considered as an upside for industrialization of ZIF-8 especially for the ones which consist of Zn and Co, thanks to its low energy cost and 1-step synthesis.

Chemicals that are used in Zn-ZIF-8 synthesis can be given as the following:
Zinc nitrate hexahydrate (98%, Alfa-Aesar) is used as a metals source. 2-methylimidazole (99%, Acros Organics) used as an organic linker and sodium formate anhydrous (purum p.a., 98%, Fluka Analytical) used as a deprotonating agent. Methanol (absolute, low acetone, 99.8%+, VWR Chemicals) is used as a solvent and Ethanol (denaturated with 3% diethlyether) for further washing.

A typical synthesis protocol includes metal salt, solvent, organic linker and modulating ligand and the applied method can be given like this. 1.4688 g (4.938 mmol) of Zn $(NO_3)_2.6H_2O$ was dissolved in 100 mL of methanol and big salt particles were broken down by ultrasound vibration. Another solution was prepared by 1.6212 g (19.748 mmol) of 2-methylimidazolate (2-mIm) and 1.343 g (19.748 mmol) of anhydrous sodium formate in 100 mL of methanol. The first solution was added to the prior solution after the prior solution became clear under stirring. Stirring action was stopped when the first solution was added to the second one. The reaction time was 24 hours and the reaction products weree either recovered by centrifugal separation or excess liquid was taken out by the pipette. The process continued with repetitive washing with ethanol and later samples were dried under 60° C in a convection oven.

Zn-ZIF-8 formation can be expressed in the following equation.

$$Zn^{2+} + 2\ (2\text{-}mIm^{-})\ Zn(2\text{-}mIm^{-}) \qquad (19)$$

The reaction rate of the formation follows as:

$$k_1\ [Zn^{2+}]\ [2\text{-}mIm^{-}]^2 \qquad (20)$$

Where, k_1 is the 3rd order rate constant [$M^{-2}\ s^{-1}$], $[Zn^{2+}]$ is the concentration of the metal salt in which zinc nitrate hexahydrate [M] and $[2\text{-}mIm^{-}]$ is 2-methylimidazolate concentration [M] [79]. Equation 18 shows that higher concentration of Zn^{2+} increases the reaction rate in a linear scale and leads to more ZIF-8 particle formation.

The effect of stirring on particle size and morphology were not investigated and preferred in the case because it has been stated that stirring can lead to huge diversities particle size which may act as a secondary nucleation of Zn-ZIF-8 [80]. In addition to that, a difference was observed in the case of excess liquid removal after the reaction. The centrifugal separation method sometimes results in agglomeration, which reduces the quality of the ZIF samples. In order to avoid that, excess liquid was removed by the pipette. Moreover, double and triple amount of starting materials were added to the same amount of solvent in order to create more ZIF-8 powders but it reduced the quality of the end product significantly and also triggered agglomeration of the powders, which can be seen in the SEM pictures below. The reason behind this is that most of the nano-sized MOF synthesis requires dilute conditions [81]. Dilution resulted in small particles even in the absence of modulating ligand [81].

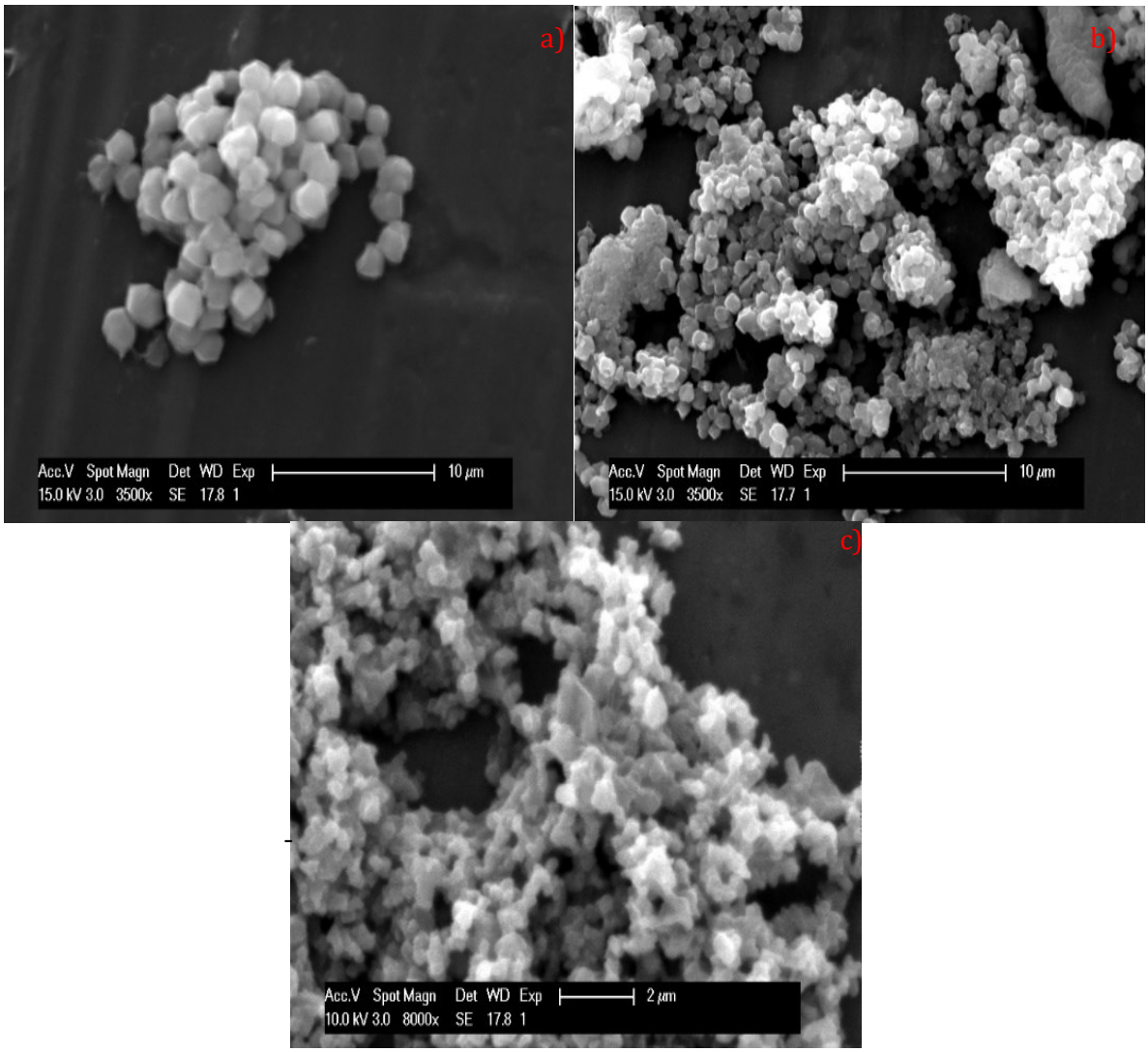

Figure 18: SEM images of Zn-ZIF-8 particles a) 1x amount of starting material, b) 2x amount of starting material, c) 3x amount of starting material

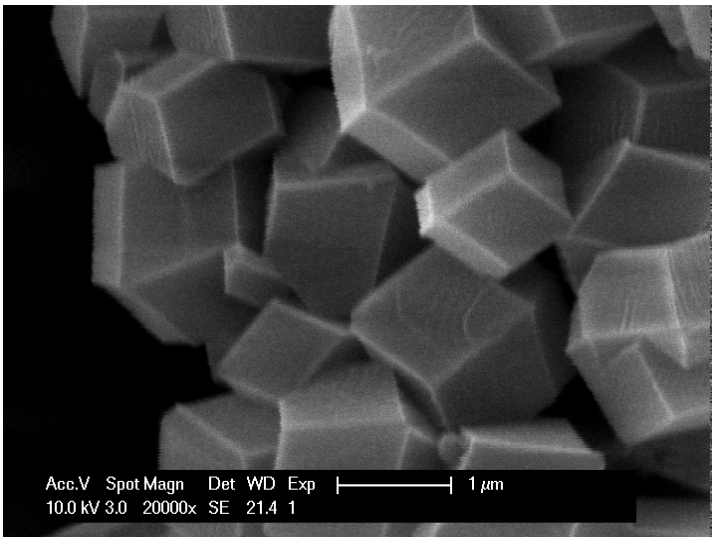

Figure 19: SEM image of Zn-ZIF-8 particles with rhombic dodecahedral structure

Rhombic dodecahedral structure can be seen easily in figure 19, which correlates with the theoretical information and also with the example image of ZIF-67 that is given in figure 17. The structure that ZIF-8 shows, called I-43m, can be defined as a body centered cubic crystal system with point group 43m [55].

When the different amounts of starting material are compared, it is definite that different ratios impact to the outcome material. The ratio of Zn salt to 2-mIm varies around 1:4 to 1:8 respectively [79]. In correspondence to that, Zn salt, 2-mIm, and methanol solvent ratio varies around 1:4:500 to 1:4:1250 [79]. If a ratio higher than 1:4:500 is used, Zn-ZIF-8 loses its morphology and results in agglomeration. Agglomeration can also be triggered by the use of centrifugal separation. This behavior in two different situations can be explained with the zeta potential of the Zn-ZIF-8 particles. Zeta potential is basically the surface charge of the particles that gives electrical stability when it is high enough and thus slows down the nucleation rate. Zeta potential is influenced mainly by the pH of the solution. This can be modified by modulators and sodium formate has been chosen for this case.

The SEM images clearly indicate the rhombic dodecahedral structure that ZIF-8 possesses and the powders are also examined with XRD analysis to discuss more about the crystalline structure. The XRD comparison of the room-temperature synthesized ZIF-8 and simulated ZIF-8 is given in figure 20.

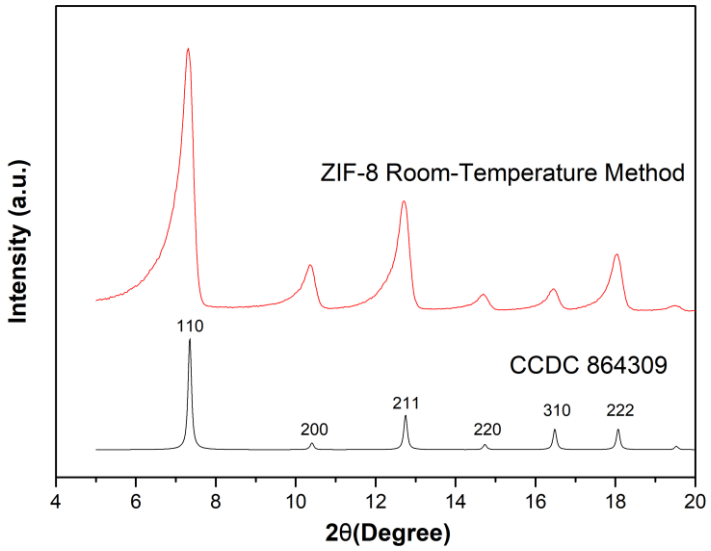

Figure 20: XRD pattern comparison with room-temperature method and simulated results (CCDC 864309). The average size of the measured particles is 1μm

As mentioned, synthesized ZIF-8 powders have a cubical structure and lattice constants are a=b=c=16.9910 Å and α=β=γ=90° with a cell volume 4905.2 $Å^3$ [55].

A comparison of diffraction patterns proved that synthesized particles are ZIF-8 with I-centered lattice. The first and sharpest diffraction peak can be seen at 7.2° and that is diffraction of carbon (110). The other diffraction lattices are also indicated in Fig 20.
Simulated XRD pattern contains much more clearly defined peaks because full crystallinity with no impurities is assumed. However, the powders synthesized with the room-temperature method are lower in crystallinity with some impurities that may have occurred because of the inadequate cleaning of both samples and equipment that are used.

The particle size of the synthesized Zn-ZIF-8 is highly important when the efficiency of the application is concerned. The smaller size particles end up having more specific area and more exposed zones to reduce oxygen which increases the efficiency of a metal-air battery. Moreover, particle size can influence the electrical properties of the end product, so precise control over size is required to obtain better results overall.

Particle size can be controlled by adjusting the amounts and ratios of used materials for the synthesis of Zn-ZIF-8, like Zn ions, the linker and modulating ligands. As the name implies, modulating ligand is the critical material since both Zn ions and organic linker are part of the building unit. The modulating ligand is used to "modulate" crystallization, pH and assembly. The hypothesis regarding modulators is that the usage of modulating agent slows down the particle formation by competing with the ligands and terminating polymerization of organic chains [82]. In addition to that, modulators adjust the pH that will lead to smaller particles. At low pH levels,

nucleation continues for a longer time because of slow deprotonation and leads to large particles [82]. The mechanism in particle size control is given by Zhang et al. in figure 2 1 [83].

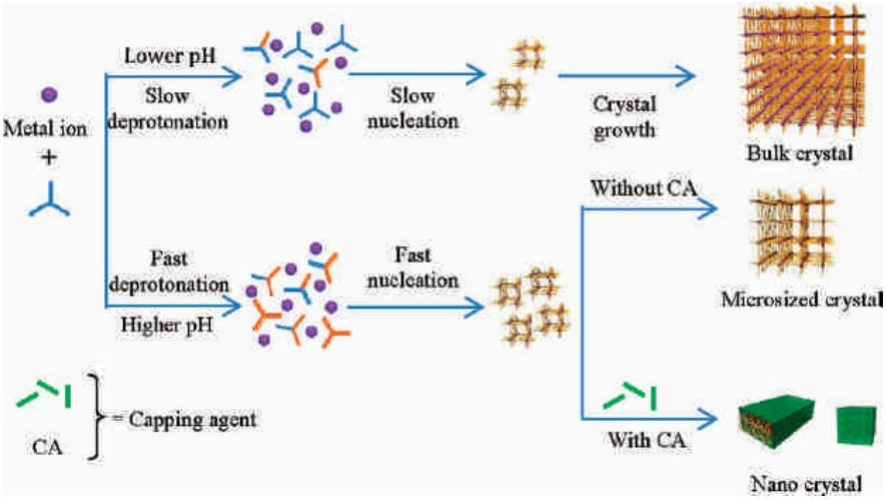

Figure 21: Effect of pH in MOF size [83]

Although the use of modulating ligands decreases the sizes of most MOF, some factors have a bigger impact than the others. In the case of Zn-ZIF-8, the addition of different modulating ligands impacted the particle size in a different way. The addition of *n*-butylamine formed nano-size crystals but in the presence of 1-methylimidazole and sodium formate micrometer sized particles are formed [80]. Particle size control with different ratios of sodium formate is investigated and a various number of powders are synthesized. The results regarding these experiments are given below.

Table 2: Relative ratio of materials and the average particle diameters of synthesized Zn-ZIF-8 particles. Particle sizes are determined by SEM

Relative ratio $Zn(NO_3)_2 \cdot 6H_2O$ / 2-mIm / sodium formate	Average particle diameter (nm)
1:4:0	80
1:4:1	300-500
1:4:2	1000-1500
1:4:3	1500-2000
1:4:4	2500-3000

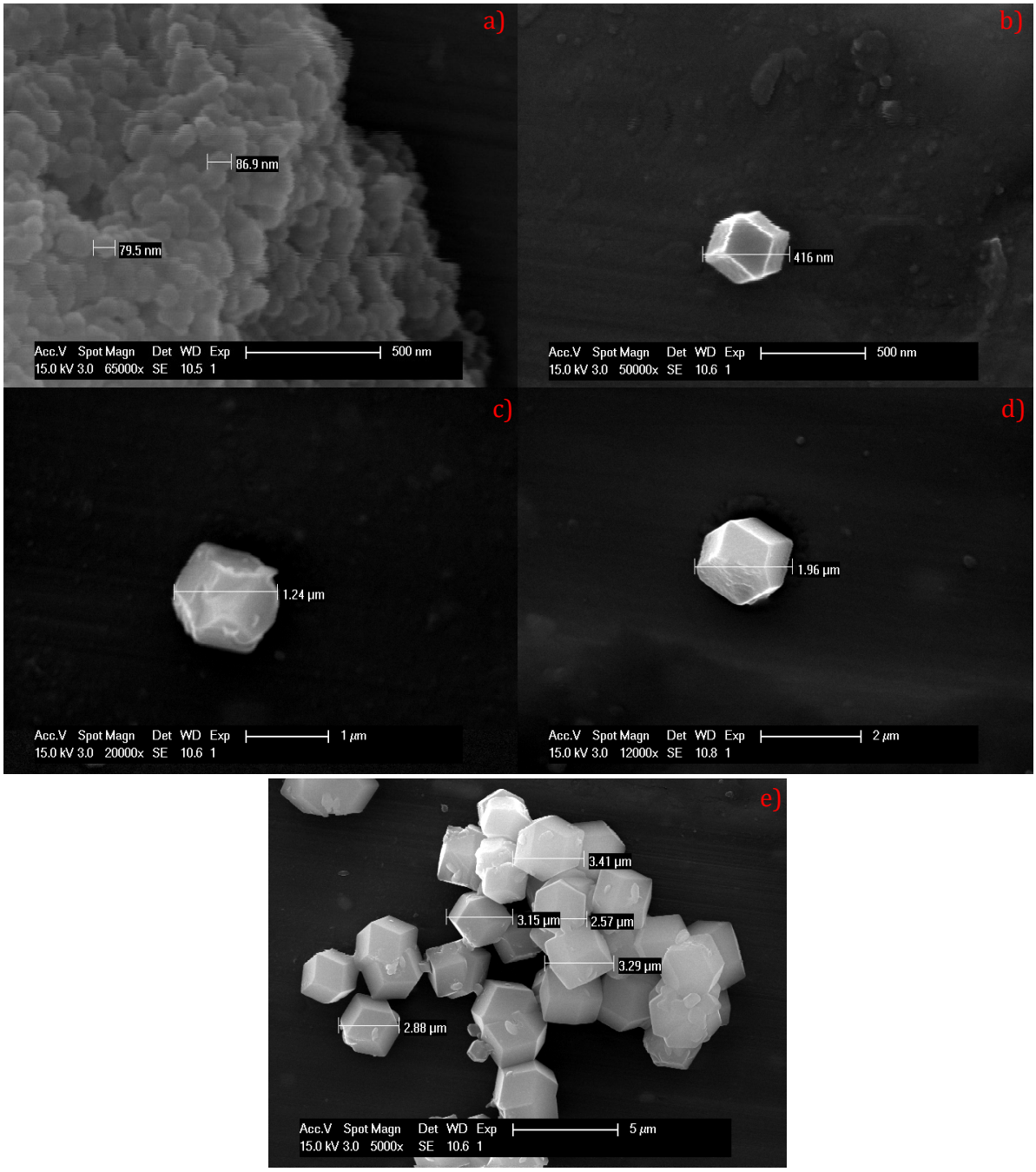

Figure 22: SEM images of Zn-ZIF-8 particles with different relative ratio a) average particle diameter 80 nm, b) average particle diameter 300-500 nm, c) average particle diameter 1-1.5 µm, d) average particle diameter 1.5-2 µm, e) average particle diameter 2.5-3.5 µm. The ratio of used Zn salt ($Zn(NO_3)_2 \cdot 6H_2O$), organic linker (2-mIm) and modulating ligand (sodium formate) is 1:4:0, 1:4:1, 1:4:2, 1:4:3, 1:4:4, respectively.

As it can be seen from the pictures provided in figure 22, increased ratio of modulating ligand resulted in an increase in the size of Zn-ZIF-8 particles. The size increase is not linear and when the modulating ligand is saturated, the excess modulating ligand is not acting as a size control mechanism but just a pH modulator. Janosch et al. stated that, the low deprotonation capability of

sodium formate is the reason of particle size increase when a higher modulating ligand to metal salt ratio is used. This comparison showed that the growth inhibition is much more crucial than the deprotonation of linker in Zn-ZIF-8 synthesis [81].

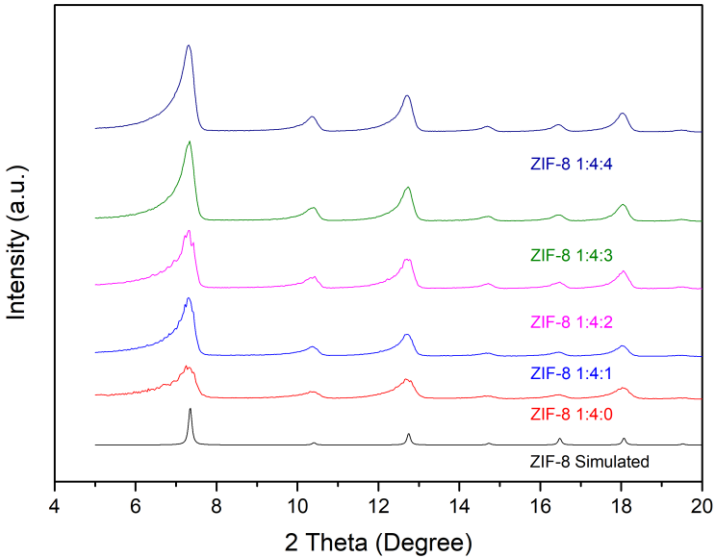

Figure 23: XRD pattern comparisons of synthesized Zn-ZIF-8 with different ratios to simulated Zn-ZIF-8 The ratio of used Zn salt ($Zn(NO_3)_2 \cdot 6H_2O$), organic linker (2-mIm) and modulating ligand (sodium formate) 1:4:0, 1:4:1, 1:4:2, 1:4:3, 1:4:4, respectively

The XRD of the samples given above is also calculated and the results are given in figure 22. As shown in the figure, all samples diffraction peaks correlate with the simulated pattern, which proves that the crystal structure of the synthesized Zn-ZIF particles is ZIF-8 crystals. In addition to that, as the sodium formate ratio increases, patterns show higher peak intensities which is the modulation effect of the ligand on specific crystal planes. Lastly, diffraction peaks are broader than the simulated pattern which means synthesized particles are less crystalline.

3.2 CdIF-1 synthesis

CdIF-1 particles carry the same structure as Zn-ZIF-8 with the only difference being that Cd atoms substitute Zn atoms. The room temperature method is also carried out to form CdIF-1 particles but no powder formation is observed. Moreover, powder formation is observed only when the temperatures are above 60° C which matches with the information given in the previous studies. CdIF-1 powder synthesis was executed solvothermally, according to the recipe given by Sun et al. [58].

Chemicals that are used in Zn-ZIF-8 synthesis can be given as the following:
Cadmium nitrate tetrahydrate (99%, Chem-Lab) is used as a metals source. 2-methylimidazole (99%, Acros Organics) is used as an organic linker and TEA (GC, T 99%, Sigma-Aldrich) is used as

a deprotonating agent. Methanol (absolute, low acetone, 99.8%+, VWR Chemicals) is used as a solvent and Ethanol (denaturated with 3% diethlyether) for further washing.

A typical synthesis protocol includes metal salt, solvent, organic linker and modulating ligand and the applied method can be given like this. 1.523 g (4.938 mmol) of Cd $(NO_3)_2.4H_2O$ was dissolved in 50 mL of methanol and big salt particles were broken down by ultrasound vibration. Another solution was prepared with 3.244 g (39.512 mmol) of 2-methylimidazolate (2-mIm) and 4 g (39.530 mmol) of TEA 50 mL of methanol. The first solution is added to the prior solution after the prior solution became clear under stirring. Stirring action continued for an hour when the first solution was added to the second one. Molar ratio of the final mixture was Cd:mIm:TEA:methanol = 1:8:8:500. The solution was transferred to a Teflon-lined autoclave and placed in a convection oven which had a constant temperature of 60° C. The reaction time was 48 hours and the reaction products were either recovered by centrifugal separation or excess liquid was taken out by the pipette. The process continued with repetitive washing with ethanol and later, samples were dried under 60° C in a convection oven.

The room synthesis method is unsuitable to be applied for CdIF synthesis. Various ratios of metal salt, organic linker and modulation ligand were tried but ZIF formation was not observed, which correlates with the findings of Sun et al. In addition to that, synthesis temperature was increased gradually and particle formation started above 60° C. The solutions that contained sodium formate were also held in a convection oven under 60° C for 1, 3 and 4 days and the resulting powders were centrifuged and washed three times. An XRD analysis of the samples was conducted and it showed that even under elevated temperatures for longer periods, sodium formate was incompetent to incorporate the organic linker with metal ions but rather connect itself. The resulting powder mainly consisted of incorporated sodium formate because of the lower solubility inside the methanol solvent which led to saturation even with smaller amount. When the solution was held more than 3 days, sodium formate incorporated with the metal ions and formed cadmium sodium formate. The experiment proves that the use of modulating ligand varies with the desired end product. Modulating ligands are crucial in ZIF synthesis and the ones that are used were already investigated. The reason behind the ineffectiveness of sodium formate in CdIF-1 synthesis can be explained by the low basicity that it possesses [84]. Thus, sodium formate is unable to deprotonate Cd^{2+} ions which can also form octahedral formation unlike the Zn^{2+} ions [85]. On the other hand, TEA has stronger basicity and deprotonates Cd^{2+} to from tetrahedral. The effect of TEA leads to agglomeration of the particles in case of Zn^{2+} due to high nucleation [86]. The effect of synthesis temperature, modulating ligand and the other factors such as the time in the furnace, equipment that is used by Sun et al. have been tested and the findings are given below.

The synthesis time under 60° C is the most important factor that determines the particle morphology and size. Other than Zn-ZIF-8, achieving the desired morphology is much more difficult since the transformation is highly complicated and this situation is sufficiently emphasized in the literature. Although there are only 2 different morphologies observed in this extensive parallel experiment and these are CdIF-1 and CdIF-3, other morphologies can be achieved when the same organic linker is used and these are CdIF-2 and CdIF-5 as listed by Tian et al. with their synthesis recipes, respectively [87]. In order to understand the effect of time on elevated temperature, various experiments with different 2-mIm to TEA ratios are executed.

The first experiment is conducted to understand the effect of furnace time on the morphology of the end powder. The corresponding XRD graph and SEM images can be seen in figure 2 4. All of the samples with the same 2-mIm to TEA ratio matched with the simulated graph, which indicates that the powder samples are pure CdIF-1. Fig. 24 b-d shows the SEM images with different furnace time. SEM images display that higher furnace time yields to bigger and more developed crystals. Fig. 24 c-d shows nano-sized CdIF-1 crystals which tend to grow on each other and thus create agglomerates.

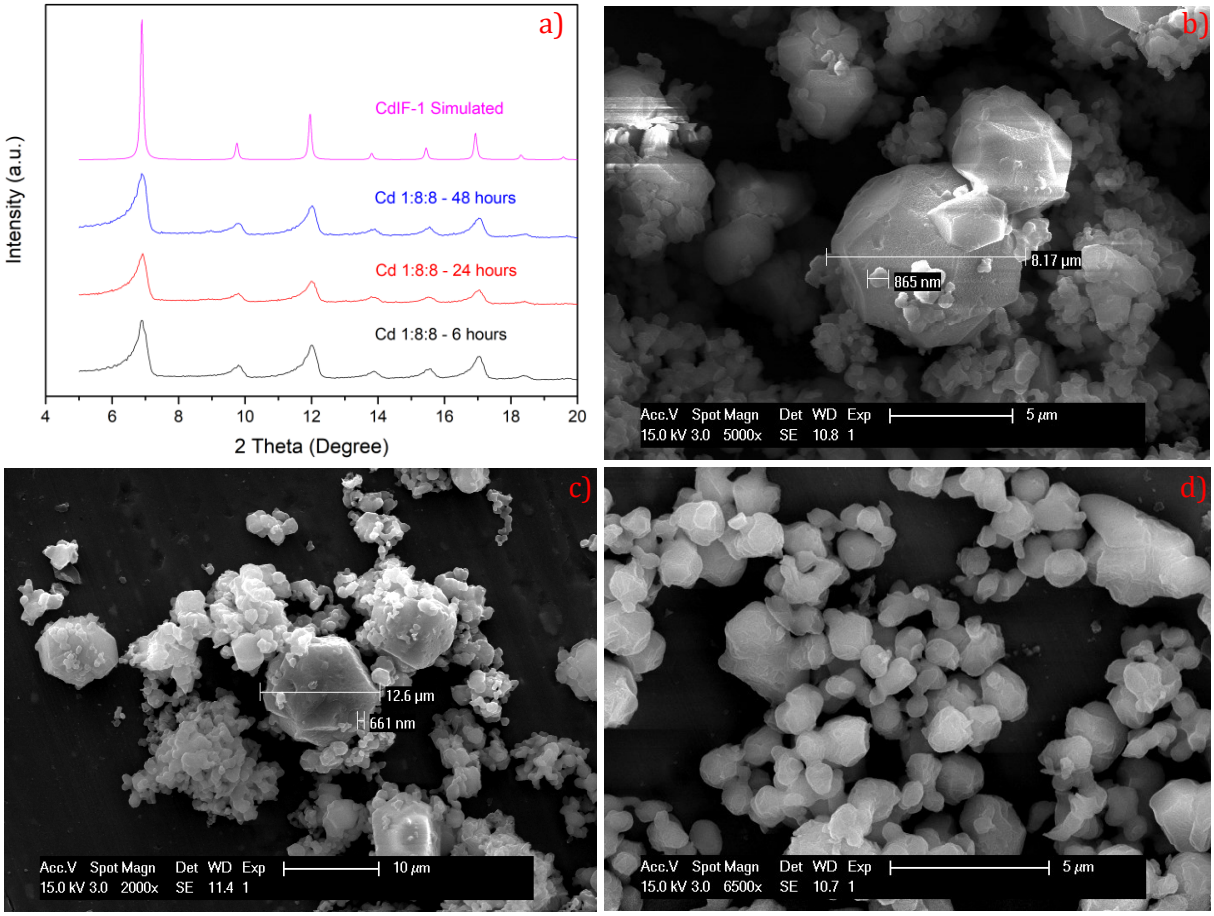

Figure 24: a) XRD pattern comparison of CdIF samples synthesized at 60° C for 6 hours, 24 hours and 48 hours with simulated CdIF-1, b), c) and d) SEM images of CdIF samples synthesized at 60° C for 6, 24 and 48 hours, respectively

After the initial experiments were held to understand the effects of synthesis time at certain temperature, different organic ligand to modulating ligand ratios were tested with the synthesis times indicated above.

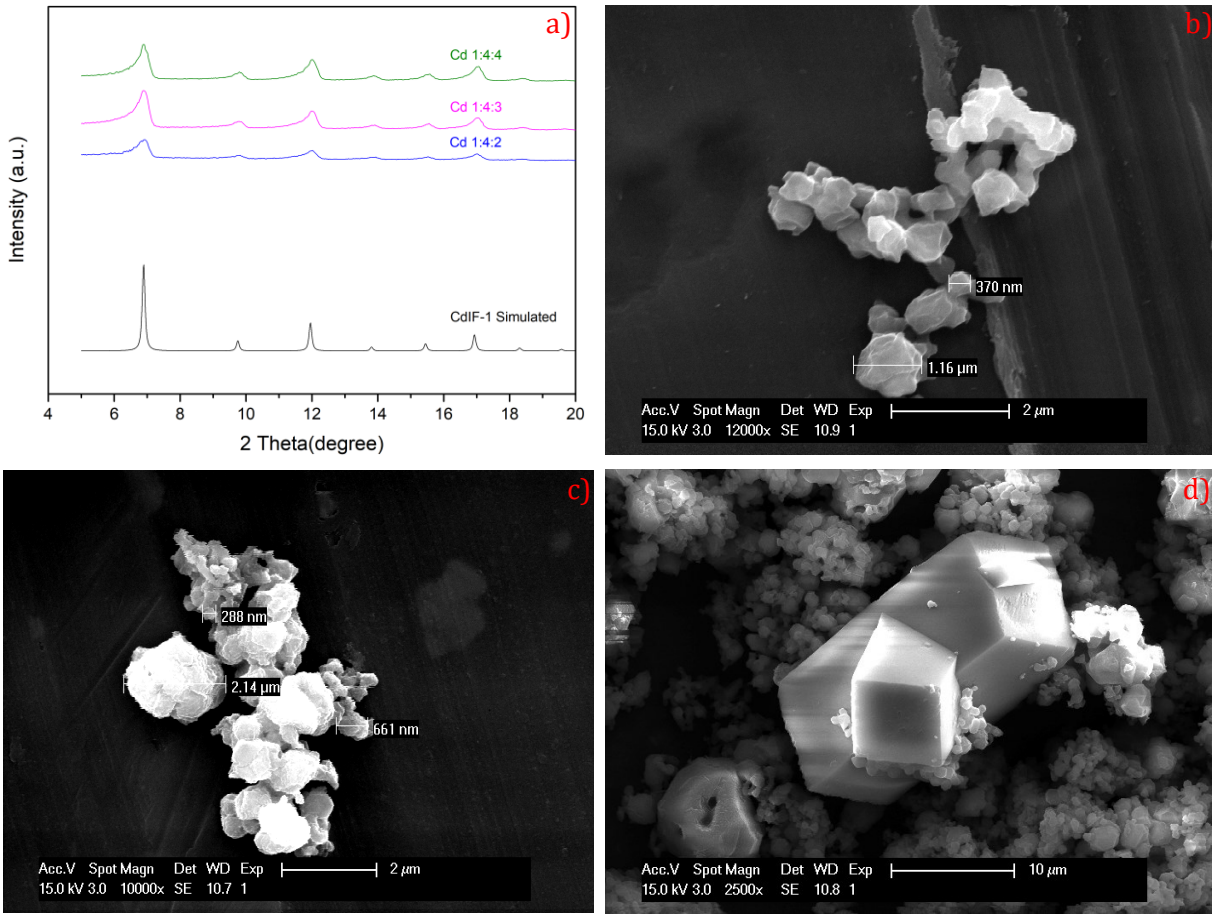

Figure 25: a) XRD pattern comparison of CdIF samples synthesized at 60° C with 2-mIm to TEA ratios of 2, 1.5 and 1 for 6 hours with simulated CdIF-1, b), c) and d) SEM images of CdIF samples synthesized at 60° C with 2-mIm to TEA ratios 1, 1.33 and 2 for 6 hours, respectively

Fig. 25 shows the powders with different 2-mIm to TEA ratios synthesized for 6 hours at 60° C. Fig. 25.a presents the XRD patterns of the synthesized powders and all of the powders follow the same pattern as the simulated one and thus the amount of TEA used in Fig 25.b is enough to obtain the desired crystal structure. As can be seen from the size of crystals in each sample, the increase in TEA amount results in bigger particles. This outcome is expected since the higher TEA amounts result in higher nucleation rates. It is worth mentioning here that figure 25.d shows two morphologies which are different from the other samples. Small CdIF-1 particles can be seen on and around the big particle which is described as CdIF-3. There was not much information available about this topology but Tian et al. described its net as **yqt1** [87]. It is also indicated that CdIF-3 is non-porous and therefore is not desired and not appropriate as a catalyst for battery applications [87]. A comparison of the XRD patterns and SEM images show that, the amount of CdIF-3 in Fig 25.d is less than 5%, which is negligible. The same experimental setup is also conducted

for a synthesis time of 24 hours and all of the resulting powder possess the XRD pattern of CdIF-1.

After CdIF-1 particles are perfectly synthesized with different 2-mIm to TEA ratios for 6 hours, a longer synthesis time period is also tested in order to understand the effect of time and the amount of TEA. As given in figure 25. a, in low organic ligand to TEA ratio, it is possible to synthesize CdIF-1 particles but the effect of lower TEA amounts on longer synthesis time periods is not available in literature explicitly. XRD pattern comparison and SEM images with respect to each composition are given in figure 26.

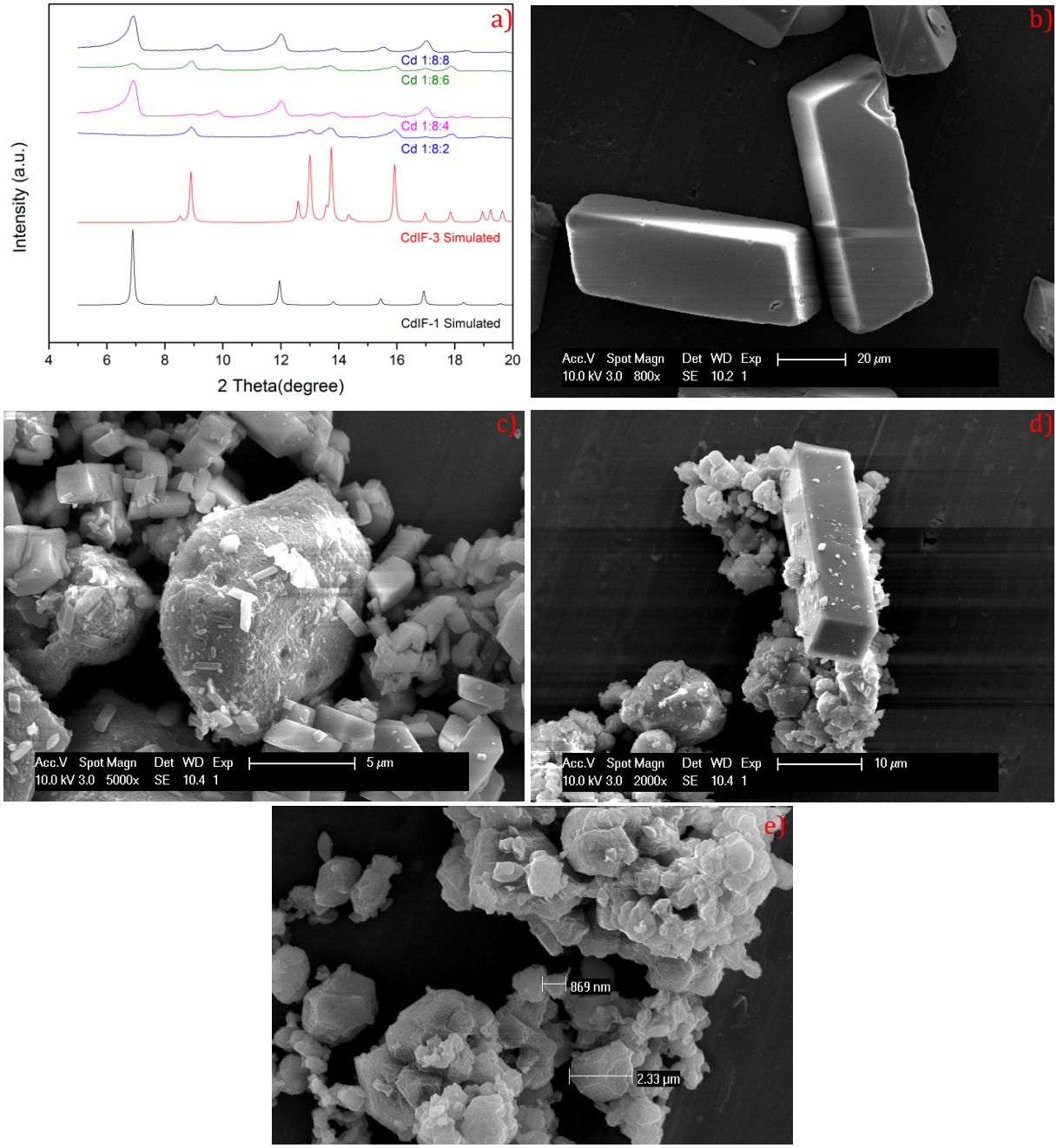

Figure 26: a) XRD pattern comparison of CdIF samples synthesized at 60° C with 2-mIm to TEA ratios of 2, 1.5, 1 and 0.5 for 2 hours with simulated CdIF-1, b), c), d) and e) SEM images of CdIF samples with 2-mIm to TEA ratios 4, 2, 1.33, and 1 for 24 hours, respectively

The amount of used TEA influenced the resulting morphologies differently when the synthesis time is further increased. XRD patterns shows that when the 2-mIm to TEA ratio is high, phase transformation from CdIF-1 to CdIF-3 is inevitable and it leads to big rectangular crystals. When 2-mIm to TEA ratio is in between 1 and 4, both of the phases are available at the same time. However, XRD patterns show that the mixture which contains a lower TEA amount has much more CdIF-1 crystals than the other mixture. In order to understand more thoroughly, SEM investigations have been made and it showed that CdIF-1 crystals are more frequent in figure 26.c, but the average size is much smaller than figure 26. As given before, when the organic linker to modulating ligand reaches 1, pure CdIF-1 crystals can be obtained. This proves that TEA is crucial for CdIF-1 synthesis as well as for the stability of the crystals in longer synthesis periods.

The effect of autoclave use is also tested in order to understand the effect of pressure on the synthesized powder. Parallel tests were executed and the results have shown that the use of autoclave does not have any significant effect on the properties of the powders. This result can be explained by the definition of solvothermal synthesis, which requires elevated temperatures higher than the boiling temperature of the solvent. In this set of experiments, methanol is used as a solvent, and the boiling temperature is given as 64-65° C by the supplier company, which is lower than the synthesis temperature of 60° C.

Lastly, the effect of stirring is investigated. In the first mixture metal salt-containing solution was added to the one which contained organic ligand and modulating ligand and mixed at 500 rpm with a magnetic stirrer for an hour. In the second mixture, metal salt-containing solution was added and both of these mixtures were placed in a convection oven for 48 hours at 60° C. Powder containing solutions were cleaned with methanol several times and centrifuged 3 times and dried overnight in a convection oven at 60° C.

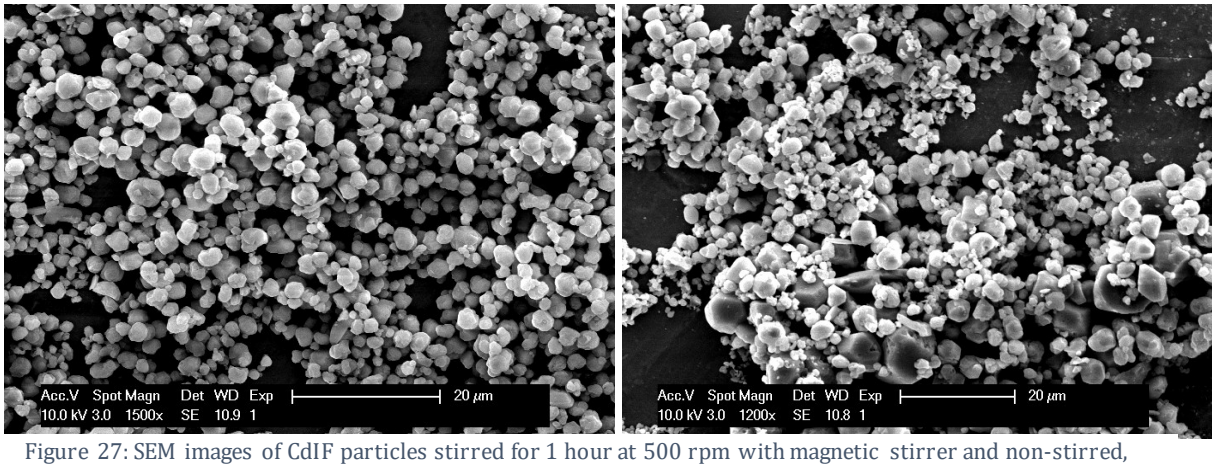

Figure 27: SEM images of CdIF particles stirred for 1 hour at 500 rpm with magnetic stirrer and non-stirred, respectively

As it can be seen from figure 27, stirring the mixture yields to a more uniform and relatively small particle size distribution. On the other hand, when the mixture is not stirred, particle size distribution is larger and not uniform. The difference between the two mixtures occurred because of the homogeneity of the solutions. The presence of TEA increases the speed of the powder formation by increasing the nucleation rate and in the more homogenous solution leads to more uniform and well-shaped powders.

After understanding the crystal forming mechanism and size control of the Zn-ZIF-8 and CdIF-1 samples, recipes that will yield a similar average particle size were chosen. These precursor materials lack conductivity, which makes it impossible to use them directly. In order to be used as a catalyst in ORR, materials require a carbonization process achieved by pyrolyzing in moderately high temperatures (750-900° C). Pyrolyzed powders contain high C content as well as low metal contents, which contributes to the reduction capabilities in electrochemical experiments.

Chapter 4. MOF driven materials

In the above work, Zn-ZIF-8 and CdIF-1 are synthesized with different parameters and similar particle size powders have been prepared. The following work is done to create a catalyst which can be used in ORR and OER. As mentioned before, MOF-driven materials possess important features required for electrochemical applications but lack of electrical conductivity makes them unsuitable to be used directly in the cathode of an air-battery. In order to create a carbon matrix which is electrically conductive, prepared powders are synthesized in different temperatures and are compared by XRD, SEM and EDS methods.

4.1. High-temperature pyrolysis of Zn-ZIF-8 and CdIF-1

Synthesized Zn-ZIF-8 and CdIF-1 particles are investigated by XRD and SEM analysis and similar particle size samples have been chosen to proceed in the next step, which is pyrolyzing of the samples. Average particle size of the chosen samples were 1-2 µm, which can be seen in the figure below.

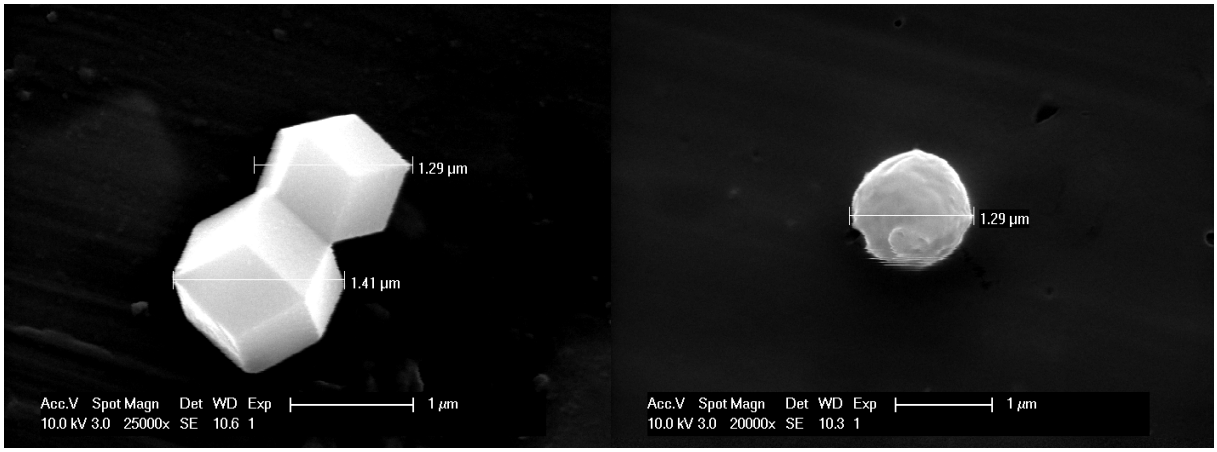

Figure 28: SEM images of pyrolyzed Zn-ZIF-8 and CdIF-1 at 750, respectively

In order to pyrolyze the samples, 6 quartz tubes with an open end with 8 mm in diameter and 10 cm in length were ordered. 300 mg of Zn-ZIF-8 and CdIF-1 were placed in the quartz tubes separately. Quartz tubes filled with powders were vacuumed and placed in a bigger quartz tube to prevent the spread of the dangerous gases which would occur during the pyrolysis. Tubes were placed in a stulp furnace which can operate up to 1000° C. Samples were heated to pyrolyzing temperature gradually with a rate of 5° C/min from room temperature and were held in that temperature for 4 hours in N_2 atmosphere with a flow rate of 300 cm^3 min^{-1}. After that samples were cooled down to room temperature with a rate of 5° C/min.

Three different temperatures are selected to pyrolyze samples and these are 750 ° C, 850° C and 900° C. Zn-ZIF-8 based materials have been investigated heavily in previous studies as a catalyst for ORR and OER and the optimal pyrolyzing temperature is found to be 900 ° C [88].

4.2. Characterization of Zn-ZIF-8 and CdIF-1 derived materials

Pyrolyzed samples were investigated using XRD, SEM and EDS point mapping methods. XRD analysis of the samples have shown that after pyrolysis in higher temperatures, the end product is carbon black. XRD patterns of pyrolyzed CdIF-1 and Zn-ZIF-8 powders are given in the figure below.

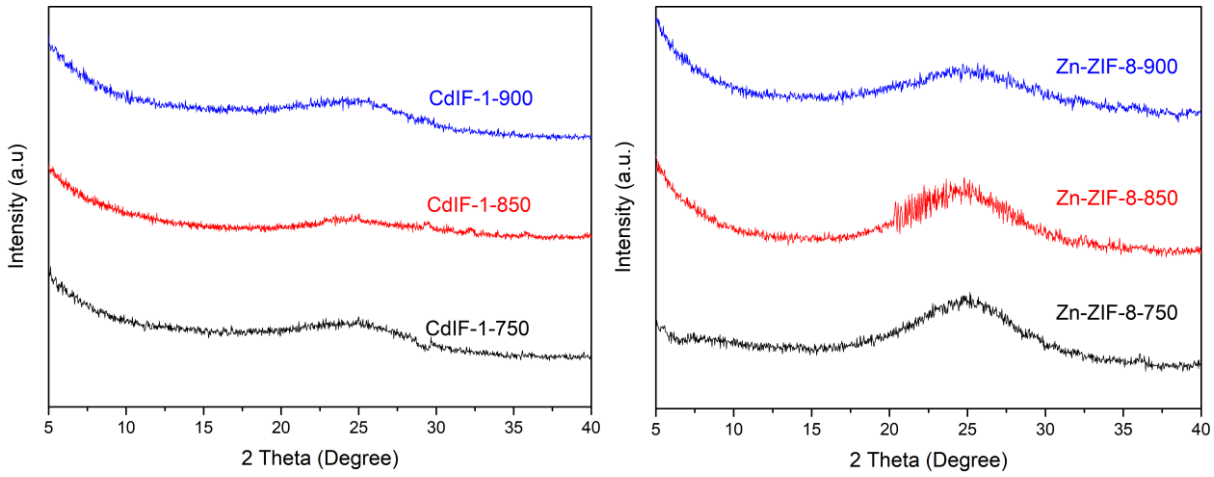

Figure 29: XRD patterns for CdIF-1 and Zn-ZIF-8 samples pyrolyzed at 750° C, 850° C and 900° C

All of the samples possess a weak, broad peak that corresponds to C (002) with no other peak and thus the pyrolyzed powders mainly consist of C [89]. It is also worth mentioning here that C peaks in Zn samples are much sharper when compared with CdIF-1, which indicates better carbonization. Further evaluation of the powders were done by the SEM and point mapping to see the morphology of the powders after pyrolysis and also to determine the remaining metal contents.

Table 3: Atomic percentage of the pyrolyzed CdIF-1 samples in different temperatures measured by EDS

Sample/Element	C	N	Cd
Cd-750	82 At%	13.93 At%	4.07 At%
Cd-850	87.65 At%	9.92 At%	2.43 At%
Cd-900	89.68 At%	8.43 At%	1.89 At%

In EDS measurements, low amounts of plating Pt and sampling surface of Al is detected and the percentages are calculated by the addition of these percentages according to the available ratio of

the elements given above. As it can be seen in the table 3, increased temperature yields to more C content while lowering Cd and N contents. A rapid decrease of Cd content was observed when pyrolyzing temperature was increased from 750° C to 850° C, because of the boiling temperature of Cd. In Zn-ZIF-8 samples, carbon content is lower than pyrolyzed CdIF-1 samples, around 70%. On the other hand, N and Zn amounts are higher, which correlates with the higher boiling temperature of Zn. Atomic percentages of pyrolyzed ZIF samples (Zn-ZIF-8 [90], Co-ZIF-67 [91] and Fe doped Zn-ZIF-8 [92]) have also shown similar relation in the literature, as the temperature increases. Atomic percentage of C and N stated as 78-80.1% and 11.9-13.2% at 800° C, respectively [90, 91]. When temperature increased to 900° C, atomic percentage of C and N stated as 87.27% and 7.12%, respectively [92]. Values retrieved from literature has shown similar atomic percentages. Higher C and N percentages in pyrolyzed CdIF-1 resulted from the boiling temperature difference between the used metal linkers.

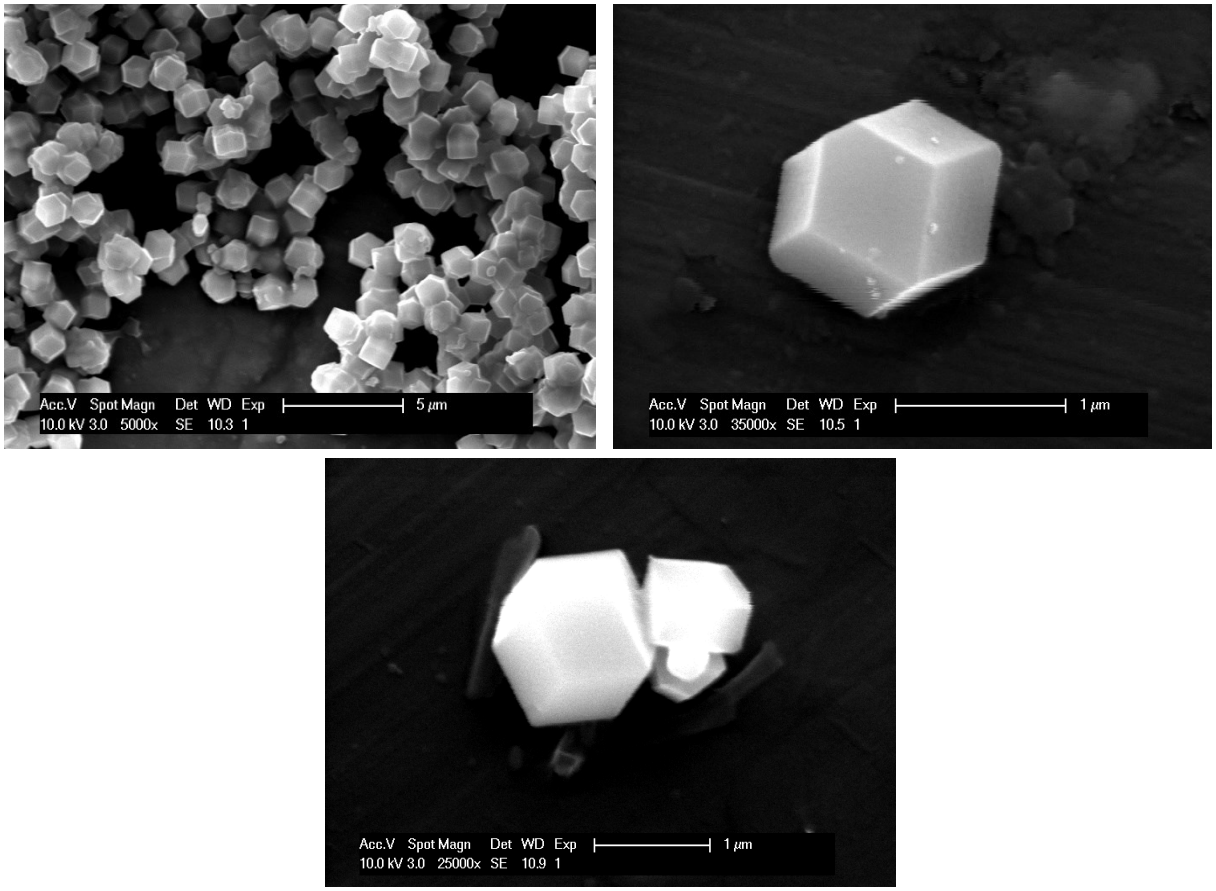

Figure 30: Zn-ZIF-8 SEM images after pyrolyzed at 750° C, 850° C and 900° C, respectively

Protection of morphology is severely important since MOF-derived materials should retain the specific surface area of the precursors. However, the specific area reduction is inevitable since some of the metal leaves the structure and reduces the area. It has been shown that in higher temperatures specific area is reduced due to the mentioned phenomena [93]. After the pyrolysis, SEM images were obtained and they showed that Zn-ZIF-8 powders fully retained ZIF-8

morphology but CdIF-1 particles lost some of the morphology. For a comparison, SEM images of CdIF-1 before and after pyrolysis were given below.

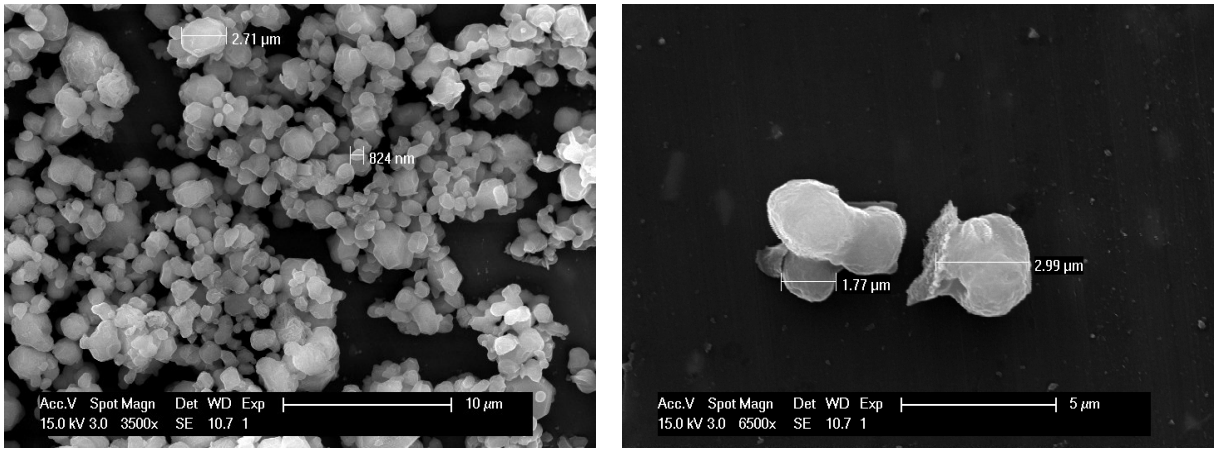

Figure 31: SEM images of CdIF-1 before and after pyrolysis at 850° C, respectively

The right particle in the second picture shows disrupted morphology, which is not visible in the precursor. Although Cd content decreased significantly as the pyrolyzing temperature increased from 750° C to 850° C, Cd is still present and this is an indication of Cd bonding with other elements since the temperature is well above the boiling temperature of Cd and duration at this temperature is fairly long, approximately 5 hours. MOFs are well-known with their sensitivity in humid conditions and this can be the main reason of morphological change occurred in pyrolyzing step [94]. It is also stated that, MOF water uptake increased suddenly when humidity is around 50%, which can lead to degradation of CdIF-1 powders [95]. Other important factor which can lead to hydrolysis is the quality of solvents used in synthesis [96]. It is also possible that, the trace oxygen present in the powder forms CdO. The decomposition of Cd MOF with imidazolate linker to various products including CdO is already mentioned in the literature when pyrolyzing temperature reached above 600 K [97]. The collapse of the framework is another option which likely to happen in higher temperatures since much more material leaves the framework and damages the stability of it. As a result, morphological change and the remaining Cd content after high pyrolysis temperatures can be explained by hydrolysis due to water uptake from air and/or low solvent quality, CdO formation due to trace oxygen and the collapse of the framework.

Another important result obtained from the SEM images of the pyrolyzed Cd samples was the phase transformation of pure CdIF-1 powders to CdIF-3. The image corresponding to this transformation is given below.

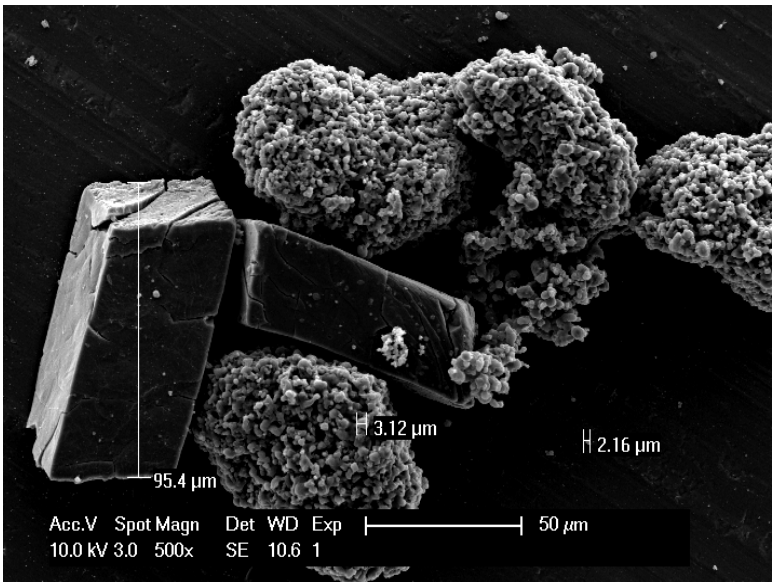

Figure 31: SEM image of CdIF-1 pyrolyzed at 750° C represents the phase transformation from CdIF-1 to CdIF-3

It was clear that the phase transformation happened during the pyrolysis of the samples, which indicates a contaminant in the precursor material. The phase transformation effect of TEA is already discussed in the previous chapter and the possibility that trace amounts of TEA remained after the extensive wash with ethanol. In order to understand the effect of contaminants available in the precursor material, half of the samples were washed 3 times more and pyrolyzed. Obtained SEM images have shown that two times washed CdIF-1 samples contain lower amounts of CdIF-3 when they are compared with the original. In addition to that, CdIF-3 particles were much smaller, which shows that a trace amount of TEA can trigger phase transformation in high temperatures.

All of the SEM images have proven that materials derived from Zn-ZIF-8 were easier to process but CdIF-1 samples were much more sensitive to phase transformation and disruption of the framework of the precursor material. For the next stage of this experiment, which is electrochemical performance test, pyrolyzed Zn-ZIF-8 and CdIF-1 samples that were washed extensively before pyrolysis were used. Prior to the electrochemical tests, powders were not washed with H_2SO_4 in order to understand the catalytic contributions of Cd and Zn metals.

Chapter 5. Electrochemical performance of MOF driven materials

The electrochemical performance of MOF-derived materials was tested by using a three-electrode cell with a rotating disc. In order to test the samples, a solution which contained 10 mg of black powder, 1 ml of ethanol and 40 µL of 5 wt%. Nafion (Alfa Aesar Germany) were added to a 1.5 ml plastic tube and these catalyst inks were sonicated for at least 30 minutes prior to the electrochemical test. Both basic and acidic electrolytes were also prepared before the tests. For the basic electrolyte, 6.6 g of KOH pellets (85%, Riedel-de Halen) was added to a 1000 ml beaker which was filled up with DI water and sonicated for 30 minutes. The same preparation procedure was also applied to the acidic electrolyte which contained 26.6 ml of H_2SO_4 (95-97% a.r., Chem-Lab) was added to 1000 ml beaker filled up with DI water. The resulting electrolyte contained 0.1M KOH and 0.5 H_2SO_4. After the sonication, 10 µL of catalyst link was loaded on a glass carbon electrode of 5 mm in diameter (loading~ 0.25 mg cm^{-2}). Before the electrochemical performance measurement, electrolytes were purged with O_2 and Ar for at least 30 minutes. Bubbling was also continued during the test moderately. The catalytic performance of the samples was measured with linear sweep voltammetry, cyclic voltammetry and electrochemical impedance spectroscopy (EIS). In order to reach and control the setup temperature, which was 25° C, an automatic thermostat was placed inside a big bowl filled up with water. This unusual setup was necessary since the room temperature was measured at 21° C and the obtained results under this condition were not appropriate to be compared with the ones available in the literature. The described setup can be seen in the figure below.

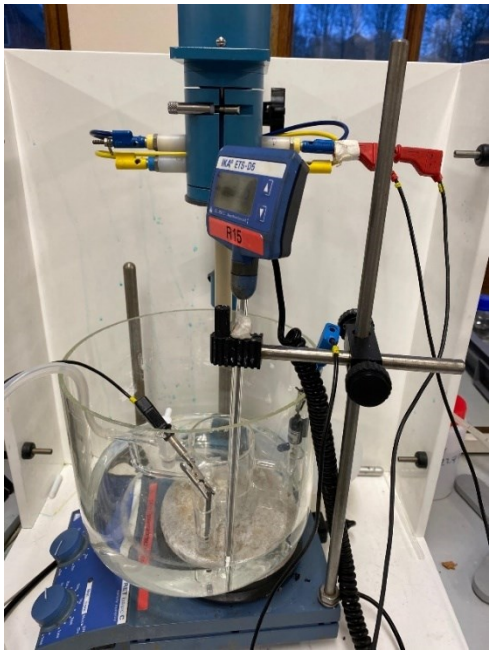

Figure 32: Electrochemical performance test actual setup

Other than rotating disc electrode in a three-electrode setup, graphene tube was used as a counter electrode and Hg/HgO and Ag/AgCl as reference electrode.

The experiment started with EIS measurements, which were recorded in a frequency range from 10^{-2} to 10^{4} Hz with a peak-to-peak amplitude of 10 mV. The experiment continued with CV for 25 cycles with 50 mV scan rate. After the cycles became steady and the catalyst was ready to give reliable results, LSV tests were conducted with a rotation speed of 400, 625, 900, 1225, 1600 and 2000. All of the applied methods were performed on an Autolab electrochemical workstation. In order to compare all of the results, the same tests were also applied to Pt/C catalyst (10% Pt, Alfa Aesar Germany) which prepared with the same ratios.

5.1. Results and Discussion

Firstly, EIS measurements were obtained in order to calculate the resistance of the samples. The important thing about the results is that the minimum resistance value is used in all of the further calculations to obtain more precise data. From this point on, the samples were referred to as Cd, Zn- the pyrolyzing temperature. The minimum resistance measured in each sample was given in the table below.

Table 4: Resistance of the samples in basic and acidic electrolytes, measured by EIS in a frequency range from 10^{-2} to 10^{4}

Sample/Electrolyte	*0.1M KOH*	*0.5M H_2SO_4*
Cd-750	14.04	3.13
Cd-850	23.41	2.42
Cd-900	22.50	4.70
Zn-750	11.83	2.43
Zn-850	14.88	3.20
Zn-900	9.98	3.25
Pt/C	24.54	3.19

It is clear that, all of the samples possess similar conductivities and similar resistances in all of the electrolytes, which makes the electrochemical results comparable. The resistance is clearly lower in the acidic electrolyte for all of the samples. The reason behind this is the Nafion added to the solution to cover the electrode surface. Nafion is used as a proton exchange membrane and it is stated that the resistance is enhanced when the pH is increased [98]. The resistances were higher than expected, thus it is possible that catalyst ink covered the electrode surface unevenly. Catalyst ink covered rotating disc electrode is given in the figure below.

Figure 33: Catalyst ink covered rotating disc electrode

After the EIS measurements, CV measurements were held to understand the catalytic activity of the prepared samples. CV of the samples were measured with a scan rate of 50 mV and each sample was cycled 25 times. Samples have shown stability after the first couple of cycles and the comparison of the last cycle is given.

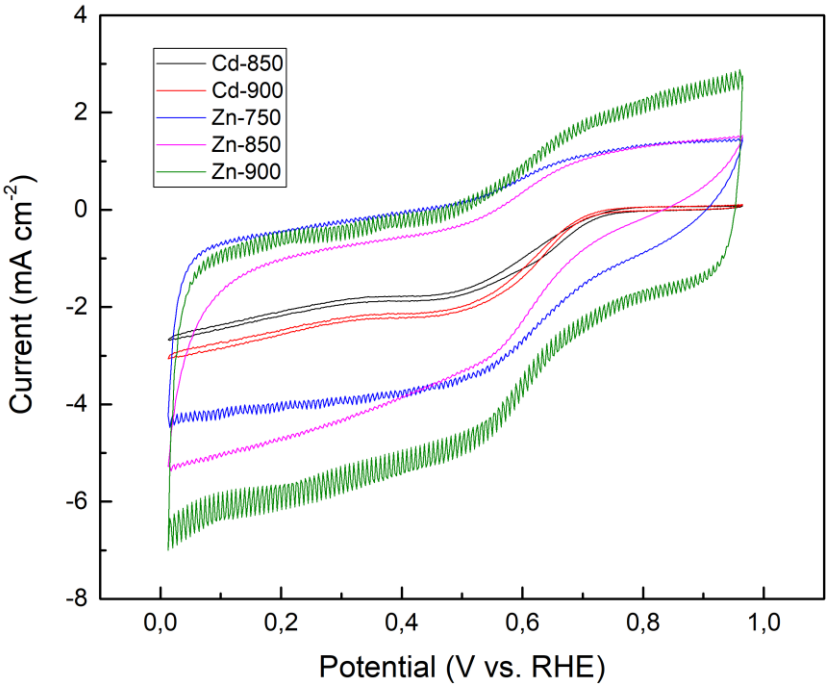

Figure 34: Last CV cycles of the samples, scanning rate is 50 mV

The CV graphs have shown that pyrolyzed CdIF-1 samples possess a much smaller area which means lower double-layer capacitance. The reason behind this behavior can be explained by the lower porosity of CdIF-1 samples when they are compared with the pyrolyzed Zn-ZIF-8. Basically, the mobility of the ions within the electrolyte is required to form a double layer [99]. The pore size is crucial in ion mobility and small size pores do not affcet double layer capacitance since they have been unable to form. Also, in the paper stated by Li et al., some of the pyrolyzed Cd powders contained low surface areas (18 m^2/g) before activation with KOH but after activation, this value ramped up to (622 m^2/g) [89]. As a result, activation with KOH prior to ORR test might increase the surface area of pyrolyzed CdIF-1 samples, thus catalytic activity in ORR. Due to this fact, the given CV graph clearly states that the pyrolyzed CdIF-1 samples contain micropores or they are non-porous. As indicated in the previous section, in the course of the pyrolyzing step, unwanted morphological and chemical changes were observed, which may lead to the reduction in porosity or even the collapse of the whole framework. The effect of porosity has been discussed already in the literature and it has been found out that higher porosity leads to more redox areas and shorter ionic diffusion distances and hence, higher charge transfer [100]. It is also worth mentioning here although more porous materials have shown better catalytic performances, the hierarchical porous structure (a combination of micro and mesopores) yields better results [101]. In the case of Zn-ZIF-8 samples, all of them have shown better catalytic performance because of their more porous structure and Zn-900 has shown the best performance due to better hierarchical pore structure.

After CV measurement lasted for 25 cycles, LSV measurements are done for all of the samples in 6 different rotation speeds and these are 400, 625, 900, 1225, 1600 and 2000 rpm. All measured potentials were converted from the Hg/HgO and Ag/AgCl electrodes using the equation given below:

$$E_{RHE} = E_{Ref.Electrode} + 0.059\text{xpH} \tag{21}$$

Where, $E_{Ref.Electrode}$ values for Hg/HgO and Ag/AgCl are 0.098 and 0.1976, pH values of electrolytes are 13 and 0.3, respectively. The calculated potentials then corrected in order to eliminate the resistance of the solution, which is given below:

$$E_{iR-corrected} = E - iR \tag{22}$$

Where i is the measured current and R is the electrolyte resistance measured by EIS at the given frequencies, which were given in table 4.

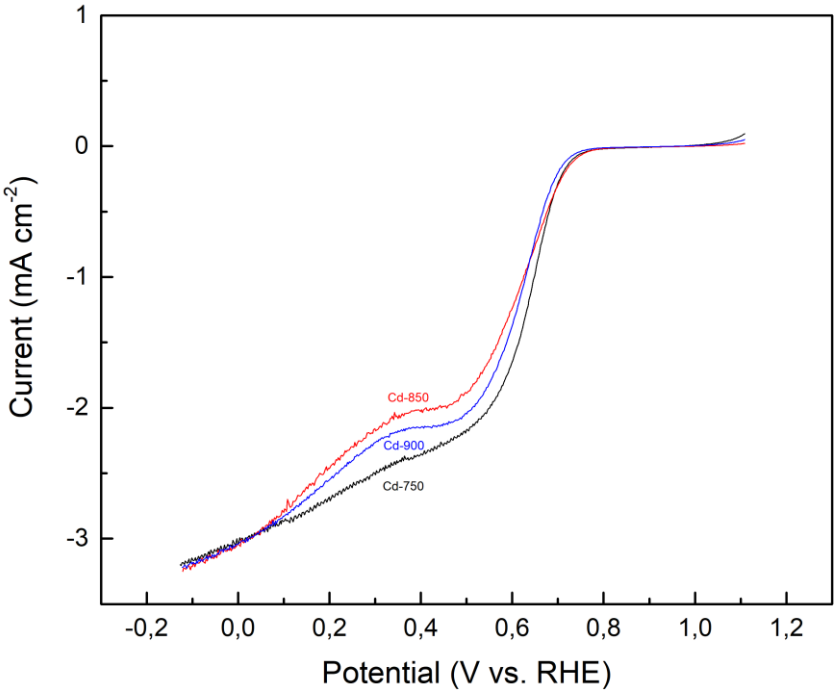

Figure 35: LSV curves of pyrolyzed Cd samples in 0.1M KOH with scan rate of 10 mV and in 1600rpm, Cd-750, Cd-850 and Cd-900 corresponds to black, red and blue lines, respectively.

Fig.36 shows the LSV curves of Cd samples at 1600 rpm with a scan rate of 10mV. It is clear from the graph that all of the samples possess similar onset potential and limiting current densities. When compared with the blank electrode, all samples have shown obvious catalytic activity for ORR [102]. In addition to that, exchange current density of the Cd-750 is higher than the other Cd samples, since it has shown much higher N contents, which can be seen from Table 4.

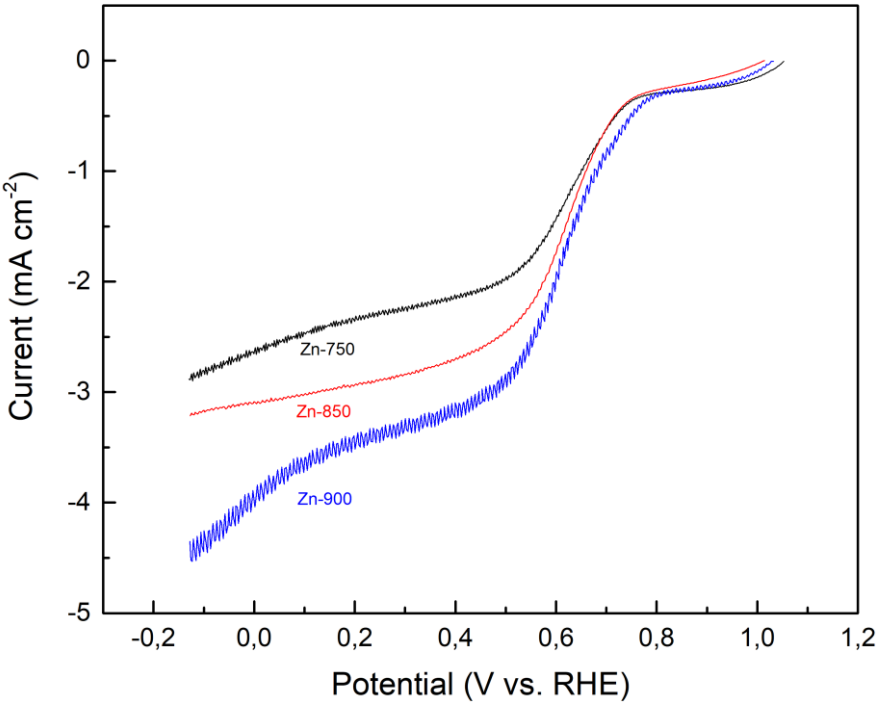

Figure 36:LSV curves of pyrolyzed Zn samples in 0.1M KOH with scan rate of 10 mV and in 1600rpm, Zn-750, Zn-850 and Zn-900 corresponds to black, red and blue lines, respectively.

LSV curves for Zn-ZIF-8 pyrolyzed at different temperatures were given in Fig.37. The limiting current density increases with temperatures significantly. Better performance of Zn-900 can be the reason for better electrochemical double-layer capacitance as a result of a larger surface area, which can be seen on the given CV cycles in Fig.35. Although surface area decreases when the temperature is increased, the incorporation of bigger pores introduces more surfaces capable of having double-layer, which might be the case for Zn-900. More detailed information about the pore structure can be obtained with Brunauer-Emmett-Teller measurement. Another reason for increased performance with increasing temperature is more graphitization occurred in higher temperatures.

Pt/C is used as a reference catalyst, which has been used as a benchmark for all catalysts in ORR applications. For comparison, samples that pyrolyzed at 750 °C were chosen, since the aim of this experiment was to obtain MOF-derived catalyst at lower temperatures than the common [72, 73]. LSV comparison of pyrolyzed Zn-ZIF-8, CdIF-1 samples and Pt/C reference catalyst were given in the figure below.

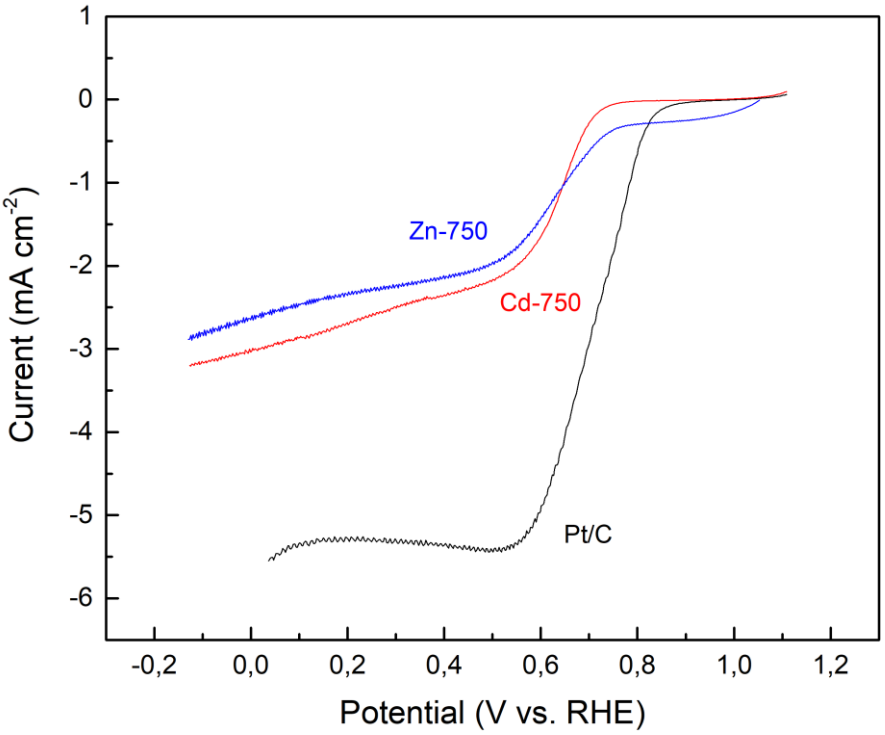

Figure 37:LSV curves of pyrolyzed Zn samples in 0.1M KOH with scan rate of 10 mV and in 1600rpm, Pt/C, Cd-750 and Zn-750 corresponds to black, red and blue lines, respectively.

The catalytic performance of Pt/C was superior when it is compared with both samples. The current density and onset potential of Pt/C is a match with the previous reports and thus, all of

the obtained results are consistent. The important thing about the performance comparison of the two catalysts is that, although Zn-750 has a better onset potential, the increase in the current density of Cd-750 was much rapid. This behavior can be explained by the slower ion access to the active surface areas. Despite this setback due to lower porosity, the limiting current density of the Cd-750 was higher than Zn-750, which shows that the catalytic activity of Cd sample was much higher.

The effect of mass transport is measured by the K-L (Koutecky-Levich) equation, which is a "powerful and versatile tool" [103]. Low enough potentials were chosen to plot K-L diagrams since, in higher absolute overpotentials, kinetics have no effect on current density. The only limiting factor is the mass transport in which Levich behavior applies. Kinetic data were calculated with the K-L equation which is given below.

$$\frac{1}{j} = \frac{1}{j_L} + \frac{1}{j_K} = \frac{1}{B\omega^{\frac{1}{2}}} + \frac{1}{nFkc_\infty} \tag{23}$$

$$B = 0.62nFD^{\frac{2}{3}}v^{-\frac{1}{6}}c_\infty \tag{24}$$

Where, $1/B$ is the slope of K-L plots, j is the obtained current density (A m^{-2}), j_L and j_K are diffusion-limited current density and kinetic current density (A m^{-2}), ω is the angular velocity of the RDE (s^{-1}), F is the Faraday constant (96,485 C mol^{-1}), D is the diffusion coefficient of O_2 in 0.1M KOH and 0.5M H_2SO_4 (1.9×10^{-9} m^2 s^{-1}) and (1.4×10^{-9} m^2 s^{-1}), v is the kinematic viscosity of the electrolytes (10^{-6} m^2 s^{-1}) and c_∞ is the bulk concentrations of O_2 in 0.1M KOH and 0.5M H_2SO_4 (1.2 mol m^{-3}) and (1.1 mol m^{-3}), respectively.

The potentials that were used to make K-L plots are -0.1V-0.05V. K-L plots of pyrolyzed Cd samples and calculated electron transfer number (n) in 0.1M KOH solution were given in Fig.39. All of the K-L plots have shown linearity and dedicated slopes were calculated with these lines. Among these catalysts, Cd-750 has shown the highest n values ($\sim$ 3.4). The electron transfer number of Pt/C catalyst is calculated as 4. In order to understand the kinetic differences of ORR between all of the samples, Tafel-plots were used. Generally, low Tafel-slope values are regarded as faster kinetics [104]. Tafel-slopes were calculated by the K-L plots given in Fig. 39 and all of the pyrolyzed Cd samples have shown low Tafel-slopes. Tafel-slopes of the pyrolyzed Cd samples are 72 mV dec^{-1}, 74 mV dec^{-1} and 71 mV dec^{-1}, respectively. Calculated Tafel-slopes were compared with Pt/C, which is 68 mV dec^{-1}. Tafel values of pyrolyzed Zn samples were also calculated and they were in the range of 200 mV dec^{-1} to 240 mV dec^{-1}, which indicates better catalytic kinetics of pyrolyzed Cd samples.

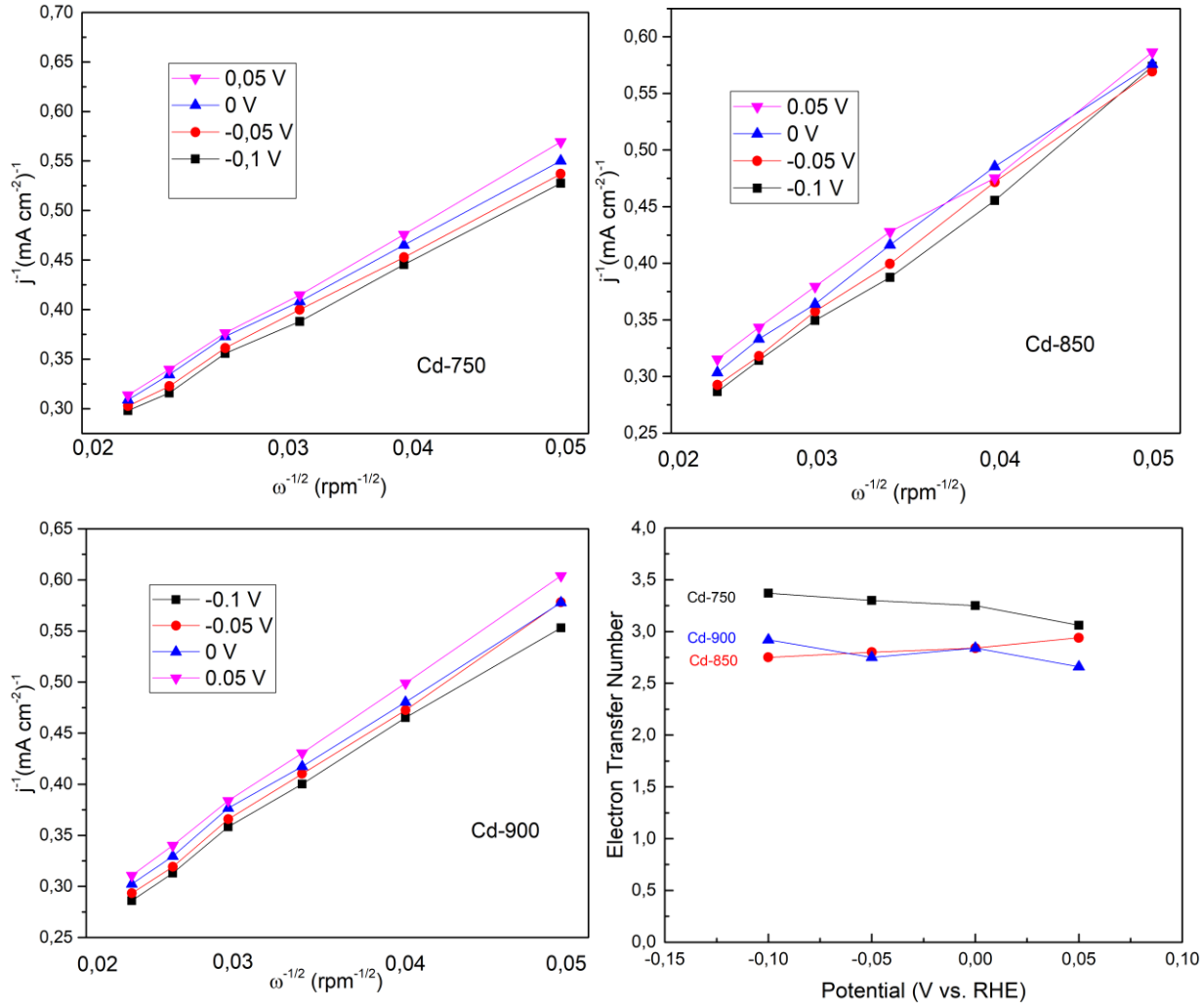

Figure 38: K-L plots of Cd-750, Cd-850 and Cd-900, electron transfer number of Cd-750, Cd-850 and Cd-900 in 0.1M KOH solution

The ORR performances of the pyrolyzed samples were also tested in 0.5 M H_2SO_4 solution in order to understand the mechanistic differences between basic and acidic media. The difference comes from the presence of OH_{ad} and the behavior against the active sites. The OH_{ad} presence blocks the direct absorption of O_2 to the active site in acidic solution [105]. On the other hand, OH_{ad} not only blocks the O_2 adsorption but also supports the outer-sphere electron transfer which makes the identity of the electrode material non-specific [105]. Thus, a wide range of non-noble electrocatalysts can be used in basic solutions but not in acidic solutions.

Pyrolyzed samples were tested in the same conditions besides the electrolyte and results have shown that the ORR performances were heavily reduced, which correlates with the information given in the literature. Moreover, the overpotentials increased rapidly. The LSV plots of Cd-750 at 1600 rpm in 0.1 MKOH and 0.5M H_2SO_4 were given below.

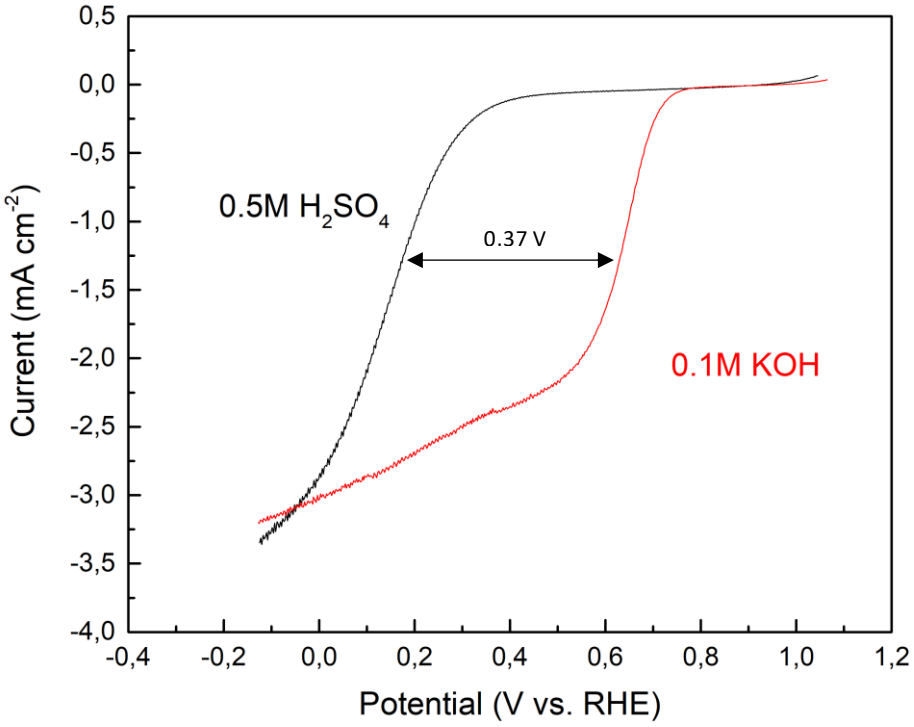

Figure 39: LSV plots of Cd-750 with a scan rate of 10mV in 0.1M KOH and 0.5M H_2SO_4 at 1600rpm, respectively

The Tafel-slopes of the pyrolyzed samples in acidic media are much higher than those in basic media. Tafel-slope values of pyrolyzed Cd samples were around 200 mV dec^{-1}, while Zn samples e showed values around 600 mV dec^{-1}. As a comparison, Tafel-slope value of Pt/C in acidic media was calculated as 33 mV dec^{-1}. Results have shown that none of the samples have good catalytic ORR kinetics in acidic media.

The OER performances of the pyrolyzed samples were also tested, but none of the samples have shown significant catalytic performances. Moreover, measured exchange current densities were much lower than the reference Pt/C catalyst, which is known with its mediocre OER performance.

Conclusion

In summary, Zn-ZIF-8 synthesis with controllable particle size was performed by adjusting the amounts of Zn-salt, organic and modulating ligands that were used. CdIF-1 synthesis was also performed and the effects of used modulating ligand, material ratio and other factors were examined and similar particle size of Zn-ZIF-8 and CdIF-1 were synthesized. Synthesized particles were characterized by using XRD and SEM. Synthesized samples were pyrolyzed in a vacuumed quartz glass in various high temperatures to see the effect of pyrolysis temperature. The pyrolyzed powders were examined by XRD, SEM and EDS to understand the final morphology and contents to support the results obtained from electrochemical tests. The electrochemical performance of the pyrolyzed samples were tested using carbon glass RDE in different media. The obtained results did not match with the predicted ones, since the collapse of the framework and hydrolysis happened in the pyrolysis step. This finding was confirmed when the CV diagrams of both pyrolyzed Zn-ZIF-8 and CdIF-1 were compared. Despite having lower surface areas, Cd samples have shown similar or better limiting current densities in moderately high temperatures. In addition to that, calculated Tafel-slope values were in the range of 71 mV dec^{-1} to 74 mV dec^{-1}, which have shown that catalytic kinetics of pyrolyzed Cd samples are on par with reference to Pt/C and much better than Zn-ZIF-8. Electron transfer values of Cd samples were better than some of the porous carbons reported in the literature, which is important as Cd samples do not possess porosity and surface area. In acidic media, none of the pyrolyzed samples have shown good catalytic performance and overpotentials increased rapidly. Lastly, OER performance of the samples were tested and obtained results were not close to Pt/C, which is known with its mediocre OER performance.

Future work

Although pyrolyzed Cd samples performed better or similar to Zn-ZIF-8 samples, the results were not satisfactory. In order to obtain clear information about possessed porosity and surface areas of pyrolyzed Cd samples, BET measurements were required. The problems related to morphological changes and the rapid reduction in surface area should be characterized deeply, to understand the mechanics behind it. Moreover, the methods mentioned in the literature in order to activate the porous carbon structure with KOH could be a possible solution to increase the surface area and porosity, which might solve the

References

[1] Wang, J., Feng, L., Tang, X., Bentley, Y., and Höök, M. 2017. The implications of fossil fuel supply constraints on climate change projections: A supply-side analysis. *Futures* 86, 58–72.

[2] Perera, F. P. 2017. Multiple Threats to Child Health from Fossil Fuel Combustion: Impacts of Air Pollution and Climate Change. *Environmental health perspectives* 125, 2, 141–148.

[3] Zhao, C., Liu, B., Piao, S., Wang, X., Lobell, D. B., Huang, Y., Huang, M., Yao, Y., Bassu, S., Ciais, P., Durand, J.-L., Elliott, J., Ewert, F., Janssens, I. A., Li, T., Lin, E., Liu, Q., Martre, P., Müller, C., Peng, S., Peñuelas, J., Ruane, A. C., Wallach, D., Wang, T., Wu, D., Liu, Z., Zhu, Y., Zhu, Z., and Asseng, S. 2017. Temperature increase reduces global yields of major crops in four independent estimates. *Proceedings of the National Academy of Sciences of the United States of America* 114, 35, 9326–9331.

[4] Owusu, P. A. and Asumadu-Sarkodie, S. 2016. A review of renewable energy sources, sustainability issues and climate change mitigation. *Cogent Engineering* 3, 1, 891.

[5] Pan, J., Xu, Y. Y., Yang, H., Dong, Z., Liu, H., and Xia, B. Y. 2018. Advanced Architectures and Relatives of Air Electrodes in Zn-Air Batteries. *Advanced science (Weinheim, Baden-Wurttemberg, Germany)* 5, 4, 1700691.

[6] The rechargeable revolution: A better battery. Retrieved December 29, 2020 from https://www.nature.com/news/the-rechargeable-revolution-a-better-battery-1.14815.

[7] Fu, J., Cano, Z. P., Park, M. G., Yu, A., Fowler, M., and Chen, Z. 2017. Electrically Rechargeable Zinc-Air Batteries: Progress, Challenges, and Perspectives. *Advanced materials (Deerfield Beach, Fla.)* 29, 7.

[8] Liu, Q., Wang, Y., Dai, L., and Yao, J. 2016. Scalable Fabrication of Nanoporous Carbon Fiber Films as Bifunctional Catalytic Electrodes for Flexible Zn-Air Batteries. *Advanced materials (Deerfield Beach, Fla.)* 28, 15, 3000–3006.

[9] Li, Y., Gong, M., Liang, Y., Feng, J., Kim, J.-E., Wang, H., Hong, G., Zhang, B., and Dai, H. 2013. Advanced zinc-air batteries based on high-performance hybrid electrocatalysts. *Nature communications* 4, 1805.

[10] Zhang, J., Zhao, Z., Xia, Z., and Dai, L. 2015. A metal-free bifunctional electrocatalyst for oxygen reduction and oxygen evolution reactions. *Nature nanotechnology* 10, 5, 444–452.

[11] Tang, C., Wang, B., Wang, H.-F., and Zhang, Q. 2017. Defect Engineering toward Atomic Co-Nx-C in Hierarchical Graphene for Rechargeable Flexible Solid Zn-Air Batteries. *Advanced materials (Deerfield Beach, Fla.)* 29, 37.

[12] Balaish, M., Kraytsberg, A., and Ein-Eli, Y. 2014. A critical review on lithium-air battery electrolytes. *Physical chemistry chemical physics: PCCP* 16, 7, 2801–2822.

[13] Lee, J.-S., Tai Kim, S., Cao, R., Choi, N.-S., Liu, M., Lee, K. T., and Cho, J. 2011. Metal-Air Batteries with High Energy Density: Li-Air versus Zn-Air. *Adv. Energy Mater.* 1, 1, 34–50.

[14] Radin, M. D. and Siegel, D. J. 2013. Charge transport in lithium peroxide: relevance for rechargeable metal–air batteries. *Energy Environ. Sci.* 6, 8, 2370.

[15] Li, Y. and Lu, J. 2017. Metal–Air Batteries: Will They Be the Future Electrochemical Energy Storage Device of Choice? *ACS Energy Lett.* 2, 6, 1370–1377.

[16] 14983913337863612 88-01899615.

[17] Peng, Z., Freunberger, S. A., Chen, Y., and Bruce, P. G. 2012. A reversible and higher-rate Li-O2 battery. *Science (New York, N.Y.)* 337, 6094, 563–566.

[18] Lee, D. U., Kim, B. J., and Chen, Z. 2013. One-pot synthesis of a mesoporous NiCo2O4 nanoplatelet and graphene hybrid and its oxygen reduction and evolution activities as an efficient bi-functional electrocatalyst. *J. Mater. Chem. A* 1, 15, 4754.

[19] Mokhtar, M., Talib, M. Z. M., Majlan, E. H., Tasirin, S. M., Ramli, W. M. F. W., Daud, W. R. W., and Sahari, J. 2015. Recent developments in materials for aluminum–air batteries: A review. *Journal of Industrial and Engineering Chemistry* 32, 1–20.

[20] Shen, K., Chen, X., Chen, J., and Li, Y. 2016. Development of MOF-Derived Carbon-Based Nanomaterials for Efficient Catalysis. *ACS Catal.* 6, 9, 5887–5903.

[21] Dhakshinamoorthy, A. and Garcia, H. 2012. Catalysis by metal nanoparticles embedded on metal-organic frameworks. *Chemical Society reviews* 41, 15, 5262–5284.

[22] Christensen, J., Albertus, P., Sanchez-Carrera, R. S., Lohmann, T., Kozinsky, B., Liedtke, R., Ahmed, J., and Kojic, A. 2011. A Critical Review of Li/Air Batteries. *J. Electrochem. Soc.* 159, 2, R1-R30.

[23] Zhang, H., Zhong, X., Shaw, J. C., Liu, L., Huang, Y., and Duan, X. 2013. Very high energy density silicide–air primary batteries. *Energy Environ. Sci.* 6, 9, 2621.

[24] H. Arai and M. Hayashi. 2009. SECONDARY BATTERIES – METAL-AIR SYSTEMS: Overview (Secondary and Primary). (December 2009).

[25] Linden, D. and Reddy, T. B. 2002. *Handbook of batteries*. McGraw-Hill handbooks. McGraw-Hill, New York.

[26] Electric vehicles and the energy sector.

[27] Zhong, Y., Xu, X., Wang, W., and Shao, Z. 2019. Recent Advances in Metal-Organic Framework Derivatives as Oxygen Catalysts for Zinc-Air Batteries. *Batteries & Supercaps* 2, 4, 272–289.

[28] Haas, O. and Van Wesemael, J. 2009. SECONDARY BATTERIES – METAL-AIR SYSTEMS: Zinc–Air: Electrical Recharge. (December 2009).

[29] Khotseng, L. 2018. Oxygen Reduction Reaction. In *Electrocatalysts for Fuel Cells and Hydrogen Evolution - Theory to Design*, A. Ray, I. Mukhopadhyay and R. K. Pati, Eds. IntechOpen. DOI=10.5772/intechopen.79098.

[30] Ma, R., Lin, G., Zhou, Y., Liu, Q., Zhang, T., Shan, G., Yang, M., and Wang, J. 2019. A review of oxygen reduction mechanisms for metal-free carbon-based electrocatalysts. *npj Comput Mater* 5, 1.
[31] SDC, S. D. Template for Electronic Submission to ACS Journals.
[32] electrocatalytic-oxygen-reduction-reaction.
[33] Anaee, R. A. M. and Abdulmajeed, M. H. 2016. Tribocorrosion. In *Advances in Tribology*, P. H. Darji, Ed. InTech. DOI=10.5772/63657.
[34] Hoogers, G. 2003. *Fuel cell technology handbook*. CRC Press, Boca Raton Fla.
[35] Joerissen, L. 2009. SECONDARY BATTERIES – METAL-AIR SYSTEMS: Bifunctional Oxygen Electrodes. (December 2009
[36] Elgrishi, N., Rountree, K. J., McCarthy, B. D., Rountree, E. S., Eisenhart, T. T., and Dempsey, J. L. 2018. A Practical Beginner's Guide to Cyclic Voltammetry. *J. Chem. Educ.* 95, 2, 197–206.
[37] epdf.pub_electrochemical-methods-fundamentals-and-applicati.
[38] Du, C., Tan, Q., Yin, G., and Zhang, J. 2014. Rotating Disk Electrode Method. In *Rotating Electrode Methods and Oxygen Reduction Electrocatalysts*. Elsevier, 171–198. DOI=10.1016/B978-0-444-63278-4.00005-7.
[39] Turick, C. E., Shimpalee, S., Satjaritanun, P., Weidner, J., and Greenway, S. 2019. Convenient non-invasive electrochemical techniques to monitor microbial processes: current state and perspectives. *Applied microbiology and biotechnology* 103, 20, 8327–8338.
[40] Tahir, M., Pan, L., Idrees, F., Zhang, X., Wang, L., Zou, J.-J., and Wang, Z. L. 2017. Electrocatalytic oxygen evolution reaction for energy conversion and storage: A comprehensive review. *Nano Energy* 37, 136–157.
[41] Chen, B., Yang, Z., Zhu, Y., and Xia, Y. 2014. Zeolitic imidazolate framework materials: recent progress in synthesis and applications. *J. Mater. Chem. A* 2, 40, 16811–16831.
[42] Mendiratta, S., Usman, M., and Lu, K.-L. 2018. Expanding the dimensions of metal–organic framework research towards dielectrics. *Coordination Chemistry Reviews* 360, 77–91.
[43] Lee, J., Farha, O. K., Roberts, J., Scheidt, K. A., Nguyen, S. T., and Hupp, J. T. 2009. Metal-organic framework materials as catalysts. *Chemical Society reviews* 38, 5, 1450–1459.
[44] Yaghi, O., Li, G. & Li, H. Selective binding and removal of guests in a microporous metal–organic framework. Nature 378, 703–706 (1995).
[45] Zhang, H., Liu, X., Wu, Y., Guan, C., Cheetham, A. K., and Wang, J. 2018. MOF-derived nanohybrids for electrocatalysis and energy storage: current status and perspectives. *Chemical communications (Cambridge, England)* 54, 42, 5268–5288.
[46] Dang, S., Zhu, Q.-L., and Xu, Q. 2018. Nanomaterials derived from metal–organic frameworks. *Nat Rev Mater* 3, 1.
[47] Liu, B., Shioyama, H., Akita, T., and Xu, Q. 2008. Metal-organic framework as a template for porous carbon synthesis. *Journal of the American Chemical Society* 130, 16, 5390–5391.
[48] Kim, H. and Lah, M. S. 2017. Templated and template-free fabrication strategies for zero-dimensional hollow MOF superstructures. *Dalton Trans.* 46, 19, 6146–6158.
[49] Phan, A., Doonan, C. J., Uribe-Romo, F. J., Knobler, C. B., O'Keeffe, M., and Yaghi, O. M. 2010. Synthesis, structure, and carbon dioxide capture properties of zeolitic imidazolate frameworks. *Accounts of chemical research* 43, 1, 58–67.
[50] Safaei, M., Foroughi, M. M., Ebrahimpoor, N., Jahani, S., Omidi, A., and Khatami, M. 2019. A review on metal-organic frameworks: Synthesis and applications. *TrAC Trends in Analytical Chemistry* 118, 401–425.
[51] Humphreys, M. N402_18c 276.279.
[52] Al-Kutubi, H., Gascon, J., Sudhölter, E. J. R., and Rassaei, L. 2015. Electrosynthesis of Metal-Organic Frameworks: Challenges and Opportunities. *CHEMELECTROCHEM* 2, 4, 462–474.
[53] Saliba, D., Ammar, M., Rammal, M., Al-Ghoul, M., and Hmadeh, M. 2018. Crystal Growth of ZIF-8, ZIF-67, and Their Mixed-Metal Derivatives. *Journal of the American Chemical Society* 140, 5, 1812–1823.
[54] Eustis, S. N., Radisic, D., Bowen, K. H., Bachorz, R. A., Haranczyk, M., Schenter, G. K., and Gutowski, M. 2008. Electron-driven acid-base chemistry: proton transfer from hydrogen chloride to ammonia. *Science (New York, N.Y.)* 319, 5865, 936–939.
[55] Park KS, Ni Z, Côté AP, Choi JY, Huang R, Uribe-Romo FJ, Chae HK, O'Keeffe M, Yaghi OM. Exceptional chemical and thermal stability of zeolitic imidazolate frameworks. Proc Natl Acad Sci U S A. 2006 Jul 5;103(27):10186-10191. doi: 10.1073/pnas.0602439103. Epub 2006 Jun 23. PMID: 16798880; PMCID: PMC1502432 .
[56] Lee, Y.-R., Jang, M.-S., Cho, H.-Y., Kwon, H.-J., Kim, S., and Ahn, W.-S. 2015. ZIF-8: A comparison of synthesis methods. *Chemical Engineering Journal* 271, 276–280.
[57] Yang, H., He, X.-W., Wang, F., Kang, Y., and Zhang, J. 2012. Doping copper into ZIF-67 for enhancing gas uptake capacity and visible-light-driven photocatalytic degradation of organic dye. *J. Mater. Chem.* 22, 41, 21849.
[58] Sun, J., Semenchenko, L., Lim, W. T., Ballesteros Rivas, M. F., Varela-Guerrero, V., and Jeong, H.-K. 2018. Facile synthesis of Cd-substituted zeolitic-imidazolate framework Cd-ZIF-8 and mixed-metal CdZn-ZIF-8. *Microporous and Mesoporous Materials* 264, 35–42.
[59] Schejn, A., Aboulaich, A., Balan, L., Falk, V., Lalevée, J., Medjahdi, G., Aranda, L., Mozet, K., and Schneider, R. 2015. Cu 2+ -doped zeolitic imidazolate frameworks (ZIF-8): efficient and stable catalysts for cycloadditions and condensation reactions. *Catal. Sci. Technol.* 5, 3, 1829–1839.
[60] Qin, J.-S., Du, D.-Y., Li, W.-L., Zhang, J.-P., Li, S.-L., Su, Z.-M., Wang, X.-L., Xu, Q., Shao, K.-Z., and Lan, Y.-Q. 2012. N-rich zeolite-like metal–organic framework with sodalite topology: high CO2 uptake, selective gas adsorption and efficient drug delivery. *Chem. Sci.* 3, 6, 2114.

[61] Hillman, F., Zimmerman, J. M., Paek, S.-M., Hamid, M. R. A., Lim, W. T., and Jeong, H.-K. 2017. Rapid microwave-assisted synthesis of hybrid zeolitic–imidazolate frameworks with mixed metals and mixed linkers. *J. Mater. Chem. A* 5, 13, 6090–6099.
[62] Xu, W., Chen, H., Jie, K., Yang, Z., Li, T., and Dai, S. 2019. Entropy-Driven Mechanochemical Synthesis of Polymetallic Zeolitic Imidazolate Frameworks for CO 2 Fixation. *Angew. Chem.* 131, 15, 5072–5076.
[63] Zhou, K., Mousavi, B., Luo, Z., Phatanasri, S., Chaemchuen, S., and Verpoort, F. 2017. Characterization and properties of Zn/Co zeolitic imidazolate frameworks vs. ZIF-8 and ZIF-67. *J. Mater. Chem. A* 5, 3, 952–957.
[64] Kadota, K., Sivaniah, E., Bureekaew, S., Kitagawa, S., and Horike, S. 2017. Synthesis of Manganese ZIF-8 from Mn(BH4)2·3THF·NaBH4. *Inorganic chemistry* 56, 15, 8744–8747.
[65] Wu, X., Liu, W., Wu, H., Zong, X., Yang, L., Wu, Y., Ren, Y., Shi, C., Wang, S., and Jiang, Z. 2018. Nanoporous ZIF-67 embedded polymers of intrinsic microporosity membranes with enhanced gas separation performance. *Journal of Membrane Science* 548, 309–318.
[66] E.C. Constable,Zinc and cadmium,Coordination Chemistry Reviews,Volume 58,1984,Pages 1-51,ISSN 0010-8545,https://doi.org/10.1016/0010-8545(84)85046-8..
[67] Baumann, A. E., Burns, D. A., Liu, B., and Thoi, V. S. 2019. Metal-organic framework functionalization and design strategies for advanced electrochemical energy storage devices. *Commun Chem* 2, 1, 1.
[68] Liu, J., Zhu, D., Guo, C., Vasileff, A., and Qiao, S.-Z. 2017. Design Strategies toward Advanced MOF-Derived Electrocatalysts for Energy-Conversion Reactions. *Adv. Energy Mater.* 7, 23, 1700518.
[69] Seo, M. H., Choi, S. M., Kim, H. J., and Kim, W. B. 2011. The graphene-supported Pd and Pt catalysts for highly active oxygen reduction reaction in an alkaline condition. *Electrochemistry Communications* 13, 2, 182–185.
[70] Li, X., Fang, Y., Lin, X., Tian, M., An, X., Fu, Y., Li, R., Jin, J., and Ma, J. 2015. MOF derived Co 3 O 4 nanoparticles embedded in N-doped mesoporous carbon layer/MWCNT hybrids: extraordinary bi-functional electrocatalysts for OER and ORR. *J. Mater. Chem. A* 3, 33, 17392–17402.
[71] Meng, Z. 2018. Bimetallic Zeolitic Imidazolate Framework-derived Porous Carbon as Efficient Bifunctional Electrocatalysts for Zn-air Battery. *Int. J. Electrochem. Sci.*, 5788–5797.
[72] Xia, B. Y., Yan, Y., Li, N., Wu, H. B., Lou, X. W., and Wang, X. 2016. A metal–organic framework-derived bifunctional oxygen electrocatalyst. *Nat Energy* 1, 1.
[73] Chen, B., Ma, G., Zhu, Y., and Xia, Y. 2017. Metal-organic-frameworks derived cobalt embedded in various carbon structures as bifunctional electrocatalysts for oxygen reduction and evolution reactions. *Scientific reports* 7, 1, 5266.
[74] Ghoshal, S., Zaccarine, S., Anderson, G. C., Martinez, M. B., Hurst, K. E., Pylypenko, S., Pivovar, B. S., and Alia, S. M. 2019. ZIF 67 Based Highly Active Electrocatalysts as Oxygen Electrodes in Water Electrolyzer. *ACS Appl. Energy Mater.* 2, 8, 5568–5576.
[75] Sung Park, K. 2016. Characterization of Zeolitic Imidazolate Framework–derived Polyhedral Carbonaceous Material and its Application to Electrocatalyst for Oxygen Reduction Reaction. *Int. J. Electrochem. Sci.*, 9295–9306.
[76] Barkholtz, H. M. and Liu, D.-J. 2017. Advancements in rationally designed PGM-free fuel cell catalysts derived from metal–organic frameworks. *Mater. Horiz.* 4, 1, 20–37.
[77] Osmieri, L. 2019. Transition Metal–Nitrogen–Carbon (M–N–C) Catalysts for Oxygen Reduction Reaction. Insights on Synthesis and Performance in Polymer Electrolyte Fuel Cells. *ChemEngineering* 3, 1, 16.
[78] Li, Y., Li, Q., Wang, H., Zhang, L., Wilkinson, D. P., and Zhang, J. 2019. Recent Progresse s in Oxygen Reduction Reaction Electrocatalysts for Electrochemical Energy Applications. *Electrochem. Energ. Rev.* 2, 4, 518–538.
[79] Beh, J. J., Lim, J. K., Ng, E. P., and Ooi, B. S. 2018. Synthesis and size control of zeolitic imidazolate framework-8 (ZIF-8): From the perspective of reaction kinetics and thermodynamics of nucleation. *Materials Chemistry and Physics* 216, 393–401.
[80] Cravillon, J., Nayuk, R., Springer, S., Feldhoff, A., Huber, K., and Wiebcke, M. 2011. Controlling Zeolitic Imidazolate Framework Nano- and Microcrystal Formation: Insight into Crystal Growth by Time-Resolved In Situ Static Light Scattering. *Chem. Mater.* 23, 8, 2130–2141.
[81] Marshall, C. R., Staudhammer, S. A., and Brozek, C. K. 2019. Size control over metal-organic framework porous nanocrystals. *Chemical science* 10, 41, 9396–9408.
[82] Forgan, R. S. 2020. Modulated self-assembly of metal–organic frameworks. *Chem. Sci.* 11, 18, 4546–4562.
[83] Guo, H., Zhu, Y., Wang, S., Su, S., Zhou, L., and Zhang, H. 2012. Combining Coordination Modulation with Acid–Base Adjustment for the Control over Size of Metal–Organic Frameworks. *Chem. Mater.* 24, 3, 444–450.
[84] Wang, F., Guo, H., Chai, Y., Li, Y., and Liu, C. 2013. The controlled regulation of morphology and size of HKUST-1 by "coordination modulation method". *Microporous and Mesoporous Materials* 173, 181–188.
[85] E.C. Constable,Zinc and cadmium,Coordination Chemistry Reviews,Volume 58,1984,Pages 1-51,ISSN 0010-8545,https://doi.org/10.1016/0010-8545(84)85046-8.
[86] Li, Y., Zhou, K., He, M., and Yao, J. 2016. Synthesis of ZIF-8 and ZIF-67 using mixed-base and their dye adsorption. *Microporous and Mesoporous Materials* 234, 287–292.
[87] Tian, Y.-Q., Yao, S.-Y., Gu, D., Cui, K.-H., Guo, D.-W., Zhang, G., Chen, Z.-X., and Zhao, D.-Y. 2010. Cadmium imidazolate frameworks with polymorphism, high thermal stability, and a large surface area. *Chemistry (Weinheim an der Bergstrasse, Germany)* 16, 4, 1137–1141.
[88] Xu, X., Hao, Z., Wang, H., Liu, J., and Yan, H. 2017. Mesoporous carbon derive d from ZIF-8 for improving electrochemical performances of commercial LiFePO 4. *Materials Letters* 197, 209–212.

[89] Li, Z.-X., Zhang, X., Liu, Y.-C., Zou, K.-Y., and Yue, M.-L. 2016. Controlling the BET Surface Area of Porous Carbon by Using the Cd/C Ratio of a Cd-MOF Precursor and Enhancing the Capacitance by Activation with KOH. *Chemistry (Weinheim an der Bergstrasse, Germany)* 22, 49, 17734–17747.
[90] Huang, L., Zhang, X., Han, Y., Wang, Q., Fang, Y., and Dong, S. 2017. In situ synthesis of ultrathin metal–organic framework nanosheets: a new method for 2D metal-based nanoporous carbon electrocatalysts. *J. Mater. Chem. A* 5, 35, 18610–18617.
[91] Chao, S., Zou, F., Wan, F., Dong, X., Wang, Y., Wang, Y., Guan, Q., Wang, G., and Li, W. 2017. Nitrogen-doped Carbon Derived from ZIF-8 as a High-performance Metal-free Catalyst for Acetylene Hydrochlorination. *Scientific reports* 7, 39789.
[92] Tran, T.-N., Shin, C.-H., Lee, B.-J., Samdani, J. S., Park, J.-D., Kang, T.-H., and Yu, J.-S. 2018. Fe–N-functionalized carbon electrocatalyst derived from a zeolitic imidazolate framework for oxygen reduction: Fe and NH 3 treatment effects. *Catal. Sci. Technol.* 8, 20, 5368–5381.
[93] Qi, Z., Pei, Y., Goh, T. W., Wang, Z., Li, X., Lowe, M., Maligal-Ganesh, R. V., and Huang, W. 2018. Conversion of confined metal@ZIF-8 structures to intermetallic nanoparticles supported on nitrogen-doped carbon for electrocatalysis. *Nano Res.* 11, 6, 3469–3479.
[94] Ming, Y., Kumar, N., and Siegel, D. J. 2017. Water Adsorption and Insertion in MOF-5. *ACS omega* 2, 8, 4921–4928.
[95] Ming, Y., Purewal, J., Yang, J., Xu, C., Soltis, R., Warner, J., Veenstra, M., Gaab, M., Müller, U., and Siegel, D. J. 2015. Kinetic Stability of MOF-5 in Humid Environments: Impact of Powder Densification, Humidity Level, and Exposure Time. *Langmuir : the ACS journal of surfaces and colloids* 31, 17, 4988–4995.
[96] Burrows, A. D., Cassar, K., Düren, T., Friend, R. M. W., Mahon, M. F., Rigby, S. P., and Savarese, T. L. 2008. Syntheses, structures and properties of cadmium benzenedicarboxylate metal-organic frameworks. *Dalton transactions (Cambridge, England : 2003),* 18, 2465–2474.
[97] Collings, I. E., Cairns, A. B., Thompson, A. L., Parker, J. E., Tang, C. C., Tucker, M. G., Catafesta, J., Levelut, C., Haines, J., Dmitriev, V., Pattison, P., and Goodwin, A. L. 2013. Homologous critical behavior in the molecular frameworks Zn(CN)2 and Cd(imidazolate)2. *Journal of the American Chemical Society* 135, 20, 7610–7620.
[98] Li, D. G., Wang, J. D., and Chen, D. R. 2014. Influence of pH value on the structure and electronic property of the passive film on 316L SS in the simulated cathodic environment of proton exchange membrane fuel cell (PEMFC). *International Journal of Hydrogen Energy* 39, 35, 20105–20115.
[99] Adam. Microsoft Word - Capstone thesis.doc.
[100] Ogale, S. B., Venkatesan, T., and Blamire, M. G., Eds. 2013. *Functional metal oxides. New science and novel applications*. Wiley-VCH Verlag GmbH & Co. KGaA, Weinheim Germany.
[101] Liang, H.-W., Zhuang, X., Brüller, S., Feng, X., and Müllen, K. 2014. Hierarchically porous carbons with optimized nitrogen doping as highly active electrocatalysts for oxygen reduction. *Nature communications* 5, 4973.
[102] Zhang, X., Luo, J., Lin, H.-F., Tang, P., Morante, J. R., Arbiol, J., Wan, K., Mao, B.-W., Liu, L.-M., and Fransaer, J. 2019. Tailor-made metal-nitrogen-carbon bifunctional electrocatalysts for rechargeable Zn-air batteries via controllable MOF units. *Energy Storage Materials* 17, 46–61.
[103] Xu, S., Kim, Y., Higgins, D., Yusuf, M., Jaramillo, T. F., and Prinz, F. B. 2017. Building upon the Koutecky-Levich Equation for Evaluation of Next-Generation Oxygen Reduction Reaction Catalysts. *Electrochimica Acta* 255, 99–108.
[104] Niu, W., Li, Z., Marcus, K., Le Zhou, Li, Y., Ye, R., Liang, K., and Yang, Y. 2018. Surface-Modified Porous Carbon Nitride Composites as Highly Efficient Electrocatalyst for Zn-Air Batteries. *Adv. Energy Mater.* 8, 1, 1701642.
[105] Ramaswamy, N. and Mukerjee, S. 2012. Fundamental Mechanistic Understanding of Electrocatalysis of Oxygen Reduction on Pt and Non-Pt Surfaces: Acid versus Alkaline Media. *Advances in Physical Chemistry* 2012, 1–17.